A 2D nonlinear multiring model for blood flow in large elastic arteries

Arthur R. Ghigo *, Jose-Maria Fullana, Pierre-Yves Lagrée

Sorbonne Universités, CNRS and UPMC Université Paris 06, UMR 7190, Institut Jean Le Rond ∂'Alembert, 4 place Jussieu, Boîte 162, 75005 Paris, France

A B S T R A C T

In this paper, we propose a two-dimensional nonlinear "multiring" model to compute blood flow in axisymmetric elastic arteries. This model is designed to overcome the numerical difficulties of three-dimensional fluid–structure interaction simulations of blood flow without using the over-simplifications necessary to obtain one-dimensional blood flow models. This multiring model is derived by integrating over concentric rings of fluid the simplified long-wave Navier–Stokes equations coupled to an elastic model of the arterial wall. The resulting system of balance laws provides a unified framework in which both the motion of the fluid and the displacement of the wall are dealt with simultaneously. The mathematical structure of the multiring model allows us to use a *finite volume* method that guarantees the conservation of mass and the positivity of the numerical solution and can deal with nonlinear flows and large deformations of the arterial wall. We show that the *finite volume* numerical solution of the multiring model provides at a reasonable computational cost an asymptotically valid description of blood flow velocity profiles and other averaged quantities (wall shear stress, flow rate, ...) in large elastic and quasi-rigid arteries. In particular, we validate the multiring model against well-known solutions such as the Womersley or the Poiseuille solutions as well as against steady boundary layer solutions in quasi-rigid constricted and expanded tubes.

© 2017 Elsevier Inc. All rights reserved.

1. Introduction

The numerical simulation of blood flow in large elastic arteries requires the resolution of a complex fluid–structure interaction (FSI) problem. Indeed, the motion of blood is governed by the three-dimensional (3D) Navier–Stokes equations for an incompressible homogeneous Newtonian fluid [1] and the deformation of the arterial wall is described by a nonlinear elastic constitutive law [2]. Several numerical methods have been proposed to solve this nonlinear 3D FSI problem [3–8]. Due to their modeling complexity and high computational cost, they have only been used to accurately compute blood flow in small regions of interest such as in arterial pathologies or small portions of the systemic network [9–11]. However, an accurate local analysis is not sufficient to obtain physiological results. Indeed, the observed waveforms in large arteries are the result of the propagation, reflection, damping and diffusion throughout the systemic network of the waves emanating from the heart [12,13]. Realistic waveforms can therefore only be computed by performing a global simulation taking into account a large portion of the arterial network. Unfortunately, such large network 3D FSI simulations are too computationally

---

* Corresponding author.
E-mail address: arthur.ghigo@dalembert.upmc.fr (A.R. Ghigo).

expensive [14]. Reduced-order models have therefore been proposed to compute physiological waveforms at lower modeling and computational costs [15–19]. The aim of this paper is to propose a novel two-dimensional (2D) reduced-order model that accurately computes linear and nonlinear blood flow features in axisymmetric rigid and elastic arteries at a reasonable computational cost with minimal modeling parameters. This model could prove to be an alternative to 3D FSI simulations in simple arterial configurations.

Reduced-order models for blood flow rely on a simplified system of equations for the motion of blood and a single equation for the deformation of the arterial wall. Assuming that the flow is axisymmetric and noticing that the characteristic length scale in the axial direction is much larger then the one in the radial direction, the Navier–Stokes equations can be simplified in the long-wave asymptotic limit. The resulting system of equations is often referred to as the reduced Navier–Stokes Prandtl (RNS-P) system of equations and a detailed derivation of this system can be found in [20,21]. This system describes the conservation of mass and the balance of axial momentum in an axisymmetric artery in which the pressure is hydrostatic (function only of the axial position x at the time t):

$$\begin{cases} \dfrac{1}{r}\dfrac{\partial}{\partial r}\left[ru_r\right] + \dfrac{\partial u_x}{\partial x} = 0 & \text{(1a)} \\[2ex] \dfrac{\partial u_x}{\partial t} + u_r\dfrac{\partial u_x}{\partial r} + u_x\dfrac{\partial u_x}{\partial x} = -\dfrac{1}{\rho}\dfrac{\partial p}{\partial x} + \dfrac{\nu}{r}\dfrac{\partial}{\partial r}\left[r\dfrac{\partial u_x}{\partial r}\right] & \text{(1b)} \\[2ex] p\left(x, r, t\right) = p\left(x, t\right). & \text{(1c)} \end{cases}$$

The axial and radial boundary conditions for system (1) are provided in the next section. Following a similar simplified approach, different hydrostatic pressure laws $p(x, t)$ can be found linking the motion of the fluid and the displacement of the wall. Depending on the problem addressed, they can describe the behavior of flexible viscoelastic rubber tubes in hydraulic systems, the propagation of a water hammer wave (Allevi's equations) or the deformation of an elastic artery. The later is used in this study and its exact formulation is given in the following section.

The RNS-P system of equations (1) is a rich dynamical system able to describe many asymptotic flow regimes in rigid tubes [22,23,21]. System (1) was solved numerically in [24,25] in a rigid axisymmetric tube using a variety of numerical methods. However, similar numerical difficulties to those encountered in 3D FSI problems arise when solving the RNS-P equations (1) in an elastic tube.

One-dimensional (1D) models were therefore introduced to simply and efficiently compute averaged quantities in elastic arteries [26–30]. These 1D models are obtained by averaging over the cross-sectional area of the artery the mass (1a) and momentum (1b) equations. Unfortunately, they depend on coefficients which themselves depend on the shape of the velocity profile, lost in the averaging process. These coefficients are therefore estimated *a priori*, which often results in unrealistic viscous dissipation and pressure losses.

One-and-a-half-dimensional (3/2D) models were then proposed as intermediary models between the too simple 1D models and too complex RNS-P equations (1) or 3D FSI systems. In [31,32], the authors used an asymptotic analysis of the RNS-P equations (1) and homogenization theory to propose a 3/2D model for blood flow in an elastic artery. This model allows to compute, without any *a priori* coefficient estimation, the zero-th and first order components of the wall displacement and the axial and radial velocities. In [33], an approximate velocity profile function was obtained depending on the instantaneous pressure gradient and the thickness of the boundary layer. This function was then used in a 1D model to compute the velocity profile-dependent coefficients. In [34], a Von Kármán–Polhausen integral method closed using the Womersley velocity profiles was studied. This integral method accurately computes linear solutions such as the Womersley solution [22] but is limited by the chosen linear closure relation. More recently, in [35], the authors proposed an analytic model for blood flow in an elastic artery based on a generalized Darcy's model and the linear Womersley theory. Despite their added modeling precision, 3/2D models still only provide approximate solutions of the RNS-P equations (1) and often rely on *a priori* unknown closure relations.

Several authors have therefore proposed numerical methods to directly solve the RNS-P equations (1) in elastic arteries. A noteworthy attempt was presented in [36] but the problem was simplified by introducing an explicit dependence with experimental data. In [34], the author derived a boundary layer method which gives good results in the linear regime but behaves poorly in the nonlinear regime. To our knowledge, the most advanced numerical method was proposed in [37]. There, a semi-implicit efficient numerical method was introduced based on an Eulerian–Lagragian method to treat the advection term and a nested Newton algorithm to iteratively compute the pressure matching the desired wall displacement. The main drawback of this approach is that it can not deal with arbitrary large wall deformation and requires that the flow stays mildly nonlinear. Additionally, the semi-implicit nature of the method results in high computational costs when considering small time steps necessary to capture wave propagation phenomena.

In this work, we therefore propose a novel 2D blood flow model to explicitly solve without any approximations the RNS-P equations (1) in elastic arteries for arbitrary large arterial wall deformations. By decomposing the fluid domain in concentric rings, we derive what we refer to as the "multiring model with mass exchange". This model is inspired from the multilayer model with mass exchange presented in [38] in the context of shallow water equations. This multiring system of balance laws provides a unified framework in which both the motion of the fluid and the displacement of the wall are dealt with simultaneously. Its mathematical structure allows us to use a *finite volume* numerical method that guarantees the
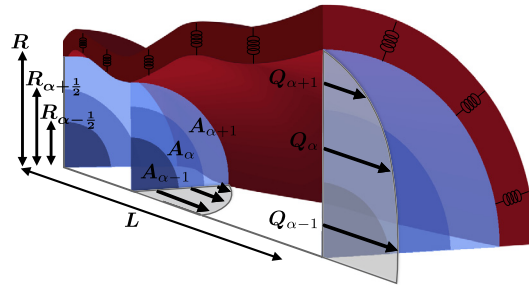
Fig. 1. Representation of the decomposition in several concentric rings of the fluid domain contained in an axisymmetric cylindrical artery. For clarity, only one-fourth of the artery of length L is represented. The springs in the arterial wall represent its elastic behavior. The variable Q_α is the flow rate in the ring α and A_α is the cross-sectional area delimited by the radii $R_{\alpha-\frac{1}{2}}$ and $R_{\alpha+\frac{1}{2}}$.

conservation of mass and the positivity of the numerical solution and can deal with nonlinear flows and large deformations of the arterial wall. We show that this multiring model can compute all relevant flow features in elastic arteries.

In the first section, we present the derivation of the multiring model. Next, we discuss its mathematical properties and details of the numerical method. In the last sections, we propose a series a examples where we compare the solution of the multiring model to analytic and reference solutions in elastic and quasi-rigid arteries.

2. A multiring discretization of the RNS-P equations

We describe a multiring model with mass exchange for blood flow based on the axisymmetric RNS-P equations (1) coupled to an elastic wall model. As stated in the introduction, this multiring model is the analog of the multilayer model with mass exchange for shallow water flows [38].

2.1. Radial decomposition of the fluid domain

In the framework of the axisymmetric RNS-P equations (1), the arteries are modeled as axisymmetric cylinders of radius R, cross-sectional area $A = \pi R^2$ and length L. In this context, the fluid region delimited by the arterial wall can be divided into N_r concentric axisymmetric rings of width h_α, with $\alpha = 1, \ldots, N_r$. To simplify the notations, we refer to the fluid ring of width h_α as the ring α. This decomposition of the fluid domain is illustrated in Fig. 1.

Each ring α is delimited by an upper and lower interface, respectively defined by the radii $R_{\alpha+\frac{1}{2}}$ and $R_{\alpha-\frac{1}{2}}$, with:

$$h_\alpha = R_{\alpha+\frac{1}{2}} - R_{\alpha-\frac{1}{2}}. \tag{2}$$

The interface position $R_{\alpha+\frac{1}{2}}$ and the radius of the artery R can now be written as:

$$R_{\alpha+\frac{1}{2}} = \sum_{j=1}^{\alpha} h_j \quad \text{and} \quad R = \sum_{j=1}^{N_r} h_j. \tag{3}$$

We also define the cross-sectional area of the ring α, noted A_α, the average flow rate in the ring α, noted Q_α, and the mean velocity in the ring α, noted u_α:

$$\begin{cases} A_\alpha = \displaystyle\int_0^{2\pi} \int_{R_{\alpha-\frac{1}{2}}}^{R_{\alpha+\frac{1}{2}}} r\,dr\,d\theta \\[3mm] Q_\alpha = \displaystyle\int_0^{2\pi} \int_{R_{\alpha-\frac{1}{2}}}^{R_{\alpha+\frac{1}{2}}} u_x r\,dr\,d\theta \\[3mm] u_\alpha = \dfrac{Q_\alpha}{A_\alpha}. \end{cases} \tag{4}$$

Finally, we note $l_{r,\alpha}$ the proportion of the total radius R occupied by the ring α:

$$h_\alpha = l_{r,\alpha} R \quad \text{with} \quad \sum_{\alpha=1}^{N_r} l_{r,\alpha} = 1, \tag{5}$$

and l_α the proportion of the total cross-sectional area A occupied by the ring α:

$$A_\alpha = l_\alpha A \quad \text{with} \quad l_\alpha = \left[\sum_{j=1}^{\alpha} l_{r,j}\right]^2 - \left[\sum_{j=1}^{\alpha-1} l_{r,j}\right]^2. \tag{6}$$

Without loss of generality, we prescribe the radial decomposition of the artery in concentric rings and set the proportion $l_{r,\alpha}$ in each ring α. This proportion is therefore a given constant number which can differ from one ring to another:

$$\forall t \geq 0, \forall x \in [0, L] \quad l_{r,\alpha} = \text{cst} \quad \text{with} \quad \alpha = 1, \ldots, N_r. \tag{7}$$

As a consequence, we have:

$$\forall t \geq 0, \forall x \in [0, L] \quad l_\alpha = \text{cst} \quad \text{with} \quad \alpha = 1, \ldots, N_r. \tag{8}$$

Assumption (7) indicates that the interfaces $R_{\alpha-\frac{1}{2}}$ and $R_{\alpha+\frac{1}{2}}$ of the ring α are not impermeable interfaces but rather interfaces of a radial mesh, and therefore mass exchanges exist between neighboring rings. This radial mesh automatically adapts itself to the movement of the arterial wall and can sustain arbitrary large wall deformation as long as $R > 0$.

In the following, we use this decomposition of the fluid domain in concentric rings to introduce a *finite volume* discretization of the axisymmetric RNS-P equations (1) in the radial direction.

2.2. System of equations for one layer

Inspired by *finite volume* methods, we integrate the axisymmetric RNS-P equations (1) over the cross-sectional area the ring α:

$$\int_0^{2\pi} \int_{R_{\alpha-\frac{1}{2}}}^{R_{\alpha+\frac{1}{2}}} \left\{ \begin{array}{l} \dfrac{1}{r}\dfrac{\partial}{\partial r}[r u_r] + \dfrac{\partial u_x}{\partial x} = 0 \\[2mm] \dfrac{\partial u_x}{\partial t} + u_r \dfrac{\partial u_x}{\partial r} + u_x \dfrac{\partial u_x}{\partial x} = -\dfrac{1}{\rho}\dfrac{\partial p}{\partial x} + \dfrac{\nu}{r}\dfrac{\partial}{\partial r}\left[r \dfrac{\partial u_x}{\partial r}\right] \end{array} \right\} r \, dr \, d\theta. \tag{9}$$

Using the Leibniz integration rule, we obtain an integral form of the axisymmetric RNS-P mass and momentum equations (resp. eq. (1a) and (1b)) in the ring α:

$$\left\{ \begin{array}{l} \dfrac{\partial A_\alpha}{\partial t} + \dfrac{\partial Q_\alpha}{\partial x} = G_{\alpha+\frac{1}{2}} - G_{\alpha-\frac{1}{2}} \\[3mm] \dfrac{\partial Q_\alpha}{\partial t} + \dfrac{\partial}{\partial x}\left[\psi_\alpha \dfrac{Q_\alpha^2}{A_\alpha}\right] + \dfrac{A_\alpha}{\rho}\dfrac{\partial p}{\partial x} = S_{M,\alpha} + S_{v,\alpha}. \end{array} \right. \tag{10a}\ \tag{10b}$$

The term $G_{\alpha+\frac{1}{2}}$ represents the radial mass exchanges at the interface $R_{\alpha+\frac{1}{2}}$ and is defined as:

$$G_{\alpha+\frac{1}{2}} = \frac{\partial}{\partial t}\left[\pi R_{\alpha+\frac{1}{2}}^2\right] + u_{x,\alpha+\frac{1}{2}}\frac{\partial}{\partial x}\left[\pi R_{\alpha+\frac{1}{2}}^2\right] - 2\pi R_{\alpha+\frac{1}{2}} u_{r,\alpha+\frac{1}{2}}, \tag{11}$$

where $u_{x,\alpha+\frac{1}{2}} = u_x\left(x, R_{\alpha+\frac{1}{2}}, t\right)$ and $u_{r,\alpha+\frac{1}{2}} = u_r\left(x, R_{\alpha+\frac{1}{2}}, t\right)$ are respectively the axial and radial velocities in $R_{\alpha+\frac{1}{2}}$. The source term $S_{M,\alpha}$ characterizes the momentum associated with the radial mass exchanges in the ring α and writes:

$$S_{M,\alpha} = u_{x,\alpha+\frac{1}{2}} G_{\alpha+\frac{1}{2}} - u_{x,\alpha-\frac{1}{2}} G_{\alpha-\frac{1}{2}}. \tag{12}$$

The source term $S_{v,\alpha}$ describes the viscous dissipation in the ring α and writes:

$$S_{v,\alpha} = 2\pi \nu \left[\left[r\frac{\partial u_x}{\partial r}\right]_{R_{\alpha+\frac{1}{2}}} - \left[r\frac{\partial u_x}{\partial r}\right]_{R_{\alpha-\frac{1}{2}}}\right]. \tag{13}$$

Finally, the nonlinear advection correction coefficient ψ_α writes:

$$\psi_\alpha = \frac{A_\alpha}{Q_\alpha^2} \int_{R_{\alpha-\frac{1}{2}}}^{R_{\alpha+\frac{1}{2}}} 2\pi r u_x^2 dr. \tag{14}$$

Up to this point, the integration process is exact and no approximation has been made in the *finite volume* radial discretization of the axisymmetric RNS-P equations (1). Next, we derive the system of equations governing the motion of blood in the entire artery.

2.3. System of equations for the artery

To obtain the system of equations governing blood flow in the entire artery, we combine the N_r system of equations (10) describing the conservation of mass and the balance of axial momentum in each ring α. The unknowns of this global system are therefore the cross-sectional area A_α and the flow rate Q_α of each ring α. However, an important consequence of assumption (7) is that the local cross-sectional area A_α can be deduced from the cross-sectional area A using the prescribed proportion l_α. The unknowns of the system are then reduced to the cross-sectional area A and the flow rate Q_α of each ring α. Indeed, by adding the N_r mass conservation equations (10a), we obtain a single mass conservation equation depending on the cross-sectional area A and the flow rate Q_α of each ring α:

$$\frac{\partial A}{\partial t} + \frac{\partial}{\partial x}\left[\sum_{j=1}^{N_r} Q_j\right] = G_{N_r+\frac{1}{2}} - G_{\frac{1}{2}}. \tag{15}$$

Performing the same operation but adding only up to the ring α, we obtain the following expression for the mass exchange term $G_{\alpha+\frac{1}{2}}$:

$$G_{\alpha+\frac{1}{2}} - \left[G_{N_r+\frac{1}{2}}\sum_{j=1}^{\alpha} l_j + G_{\frac{1}{2}}\sum_{j=\alpha+1}^{N_r} l_j\right] = \sum_{j=1}^{\alpha}\left[\frac{\partial Q_j}{\partial x} - l_j\sum_{p=1}^{N_r}\left[\frac{\partial Q_p}{\partial x}\right]\right]. \tag{16}$$

Combining the previous remarks, we obtain a global system of equations describing the conservation of mass in the artery and the balance of axial momentum in each ring α. We refer to this system as the multiring system of equations, which depends on the variables $\left[A, Q_1, \ldots, Q_\alpha, \ldots, Q_{N_r}, p\right]$ and writes:

$$\begin{cases} \dfrac{\partial A}{\partial t} + \dfrac{\partial}{\partial x}\left[\displaystyle\sum_{j=1}^{N_r} Q_j\right] = G_{N_r+\frac{1}{2}} - G_{\frac{1}{2}} & \text{(17a)} \\[4mm] \dfrac{\partial Q_\alpha}{\partial t} + \dfrac{\partial}{\partial x}\left[\psi_\alpha \dfrac{Q_\alpha^2}{l_\alpha A}\right] + l_\alpha \dfrac{A}{\rho}\dfrac{\partial p}{\partial x} = S_{M,\alpha} + S_{v,\alpha} \quad \text{for} \quad \alpha = 1, \ldots, N_r. & \text{(17b)} \end{cases}$$

We now provide a closure relation linking the pressure p with the cross-sectional area A and describing the elastic behavior of the arterial wall.

2.4. Pressure law

We assume that the artery is an incompressible, isotropic and homogeneous thin-walled elastic cylinder and that each section of the wall moves independently of the others. Under these hypotheses, the transmural hydrostatic pressure can be expressed as:

$$p(x,t) - p_0 = K(x)\left(\sqrt{A(x,t)} - \sqrt{A_0(x)}\right). \tag{18}$$

See [39,28–30] for details. The variables A_0 and K respectively represent the neutral cross-sectional area (when there is no flow) and the arterial wall rigidity. Both can vary with the axial position x. The variable p_0 is the pressure applied on the exterior of the arterial wall and is assumed constant in the following.

2.5. Radial boundary conditions

To complete the description of the system of equations (17), we provide boundary conditions at center of the artery, in $r = R_{\frac{1}{2}} = 0$, and at the arterial wall, in $r = R_{N_r+\frac{1}{2}} = R$.

In the center of the artery, in $r = R_{\frac{1}{2}}$, the velocity verifies the following axisymmetric boundary conditions:

$$\left.\frac{\partial u_x}{\partial r}\right|_{R_{\frac{1}{2}}} = 0 \quad \text{and} \quad u_r|_{R_{\frac{1}{2}}} = 0. \tag{19}$$

At the arterial wall, in $r = R_{N_r+\frac{1}{2}}$, the following classical kinematic boundary condition is verified stating that the arterial wall is a material interface:

$$2\pi R_{N_r+\frac{1}{2}} u_{r,N_r+\frac{1}{2}} - \frac{\partial}{\partial t}\left[\pi R_{N_r+\frac{1}{2}}^2\right] - u_{x,N_r+\frac{1}{2}}\frac{\partial}{\partial x}\left[\pi R_{N_r+\frac{1}{2}}^2\right] = 0. \tag{20}$$

Since we have assumed that each section of the wall moves independently of the others, which is a consequence of the fact that the axial stress at the wall is negligible compared to the radial stress, the following no-slip boundary conditions is also verified at the arterial wall, in $r = R_{N_r + \frac{1}{2}}$:

$$u_{x, N_r + \frac{1}{2}} = 0. \tag{21}$$

As a result, the expressions of mass exchange terms $G_{\frac{1}{2}}$ and $G_{N_r + \frac{1}{2}}$ can be simplified using the boundary conditions (19) and (20):

$$G_{\frac{1}{2}} = 0 \quad \text{and} \quad G_{N_r + \frac{1}{2}} = 0. \tag{22}$$

Equations (22) indicate that there is no mass exchange at the arterial wall due to its impermeability and that there is no mass exchange in the center of the artery due to the axisymmetry of the flow.

2.6. Multiring system of equations

Injecting the pressure law (18) and the boundary conditions (22) in the multiring system of equations (17), we obtain the final closed-form of the multiring equations describing the conservation of mass and the balance of axial momentum in an elastic impermeable axisymmetric artery:

$$
\begin{cases}
\dfrac{\partial A}{\partial t} + \dfrac{\partial F_A}{\partial x} = 0 & \text{(23a)} \\[2mm]
\dfrac{\partial Q_\alpha}{\partial t} + \dfrac{\partial F_{Q_\alpha}}{\partial x} = S_{M,\alpha} + S_{v,\alpha} + l_\alpha S_T \quad \text{for} \quad \alpha = 1, \dots, N_r, & \text{(23b)}
\end{cases}
$$

where:

$$
\begin{cases}
F_A = \displaystyle\sum_{j=1}^{N_r} Q_j & \text{(24a)} \\[3mm]
F_{Q_\alpha} = \psi_\alpha \dfrac{Q_\alpha^2}{l_\alpha A} + l_\alpha \dfrac{K}{3\rho} A^{\frac{3}{2}}, & \text{(24b)}
\end{cases}
$$

and:

$$S_T = \frac{A}{\rho} \left[\frac{\partial}{\partial x} \left[K \sqrt{A_0} \right] - \frac{2}{3} \sqrt{A} \frac{\partial K}{\partial x} \right]. \tag{25}$$

The source term S_T is the geometrical and mechanical source term and is non-zero when the neutral cross-sectional area A_0 or the arterial wall rigidity K vary with the axial position x. The mass exchange source term $S_{M,\alpha}$ is defined by expression (12) and the viscous source term by expression (13). The expression (16) for the mass exchange term $G_{\alpha + \frac{1}{2}}$ in each ring α can be simplified using the boundary conditions (22) and writes:

$$G_{\alpha + \frac{1}{2}} = \sum_{j=1}^{\alpha} \left[\frac{\partial Q_j}{\partial x} - l_j \sum_{p=1}^{N_r} \left[\frac{\partial Q_p}{\partial x} \right] \right]. \tag{26}$$

In the remainder of the study, we assume that the advection correction coefficient $\psi_\alpha = 1$ in each ring α. Doing so, we suppose that the velocity profile is a piece-wise constant function of the variable r. This classical *finite volume* hypothesis is the only one used in the derivation of the multiring system of equations starting from the RNS-P equations (1) and is reasonable if we use a sufficiently large number of rings N_r.

2.7. Radial velocity

In the derivation of the multiring system of equations (23), the radial velocity u_r has been eliminated from the RNS-P equations (1) through the successive radial integration of the incompressibility equation (1a) (see equation (10a)) and the manipulation of the mass exchange term $G_{\alpha + \frac{1}{2}}$ (11) (see equation (16)). However, we can post-process the radial velocity u_r by integrating the incompressibility equation (1a) over the cross-sectional area of the ring α, which gives:

$$[ru_r]_{R_{\alpha+\frac{1}{2}}} = [ru_r]_{R_{\alpha-\frac{1}{2}}} - \int_{R_{\alpha-\frac{1}{2}}}^{R_{\alpha+\frac{1}{2}}} r \frac{\partial u_x}{\partial x} dx. \tag{27}$$

Using the axisymmetric boundary condition (19), which writes:

$$u_{r,\frac{1}{2}} = 0, \tag{28}$$

and a numerical approximation of equation (27), we then iteratively compute the radial velocity $u_{r,\alpha+\frac{1}{2}}$ in each ring α. We finally obtain an approximation of the average radial velocity $u_{r,\alpha}$ in the ring α as:

$$u_{r,\alpha} = \frac{u_{r,\alpha-\frac{1}{2}} + u_{r,\alpha+\frac{1}{2}}}{2}. \tag{29}$$

2.8. Link with the one-dimensional blood flow equations

The multiring system of equations (23) is a generalization of the classical 1D system of equations for blood flow. Indeed, by adding the momentum conservation equations (23b) of all the rings α, we obtain the following global momentum conservation equation:

$$\frac{\partial Q}{\partial t} + \frac{\partial}{\partial x} \left[\sum_{\alpha=1}^{N_r} F_{Q_\alpha} \right] = \sum_{\alpha=1}^{N_r} \left[S_{M,\alpha} + S_{v,\alpha} + l_\alpha S_T \right], \tag{30}$$

where:

$$Q = \sum_{\alpha=1}^{N_r} Q_\alpha. \tag{31}$$

Using the boundary conditions (22), equation (30) simplifies to:

$$\frac{\partial Q}{\partial t} + \frac{\partial}{\partial x} \left[\left[\sum_{\alpha=1}^{N_r} \frac{Q_\alpha^2}{l_\alpha A} \right] + \frac{K}{3\rho} A^{\frac{3}{2}} \right] = 2\pi \nu \left[r \frac{\partial u_x}{\partial r} \right]_{R_{N_r+\frac{1}{2}}} + S_T. \tag{32}$$

Combining the mass conservation equation (23a) with equation (32), we obtain the following 1D system of equations for blood flow, describing the conservation of mass and the balance of axial momentum in an elastic artery:

$$\begin{cases} \dfrac{\partial A}{\partial t} + \dfrac{\partial Q}{\partial x} = 0 & (33a) \\[3mm] \dfrac{\partial Q}{\partial t} + \dfrac{\partial}{\partial x} \left[\left[\displaystyle\sum_{\alpha=1}^{N_r} \dfrac{Q_\alpha^2}{l_\alpha A} \right] + \dfrac{K}{3\rho} A^{\frac{3}{2}} \right] = 2\pi \nu \left[r \dfrac{\partial u_x}{\partial r} \right]_{R_{N_r+\frac{1}{2}}} + S_T. & (33b) \end{cases}$$

The remaining unknowns are the nonlinear advection term $\sum_{\alpha=1}^{N_r} Q_\alpha^2 / [l_\alpha A]$ and the viscous term $2\pi \nu [r\partial_r u_x]_{R_{N_r+\frac{1}{2}}}$. They depend of the shape of the axial velocity profile $u_x(x, r, t)$, which is lost in the averaging process. It is therefore classical to close system (33) by prescribing an *a priori* shape of the velocity profile. As an example, if we assume that the velocity profile is a Poiseuille profile, we have as in [40]:

$$\sum_{\alpha=1}^{N_r} \frac{Q_\alpha^2}{l_\alpha A} \approx \frac{4}{3} \frac{Q^2}{A} \quad \text{and} \quad 2\pi \nu \left[r \frac{\partial u_x}{\partial r} \right]_{R_{N_r+\frac{1}{2}}} = -8\pi \nu \frac{Q}{A}. \tag{34}$$

Unfortunately, in the vast majority of flow configurations, this *a priori* shape is an unknown function of time and position and the correct estimation of the coefficients $\sum_{\alpha=1}^{N_r} Q_\alpha^2 / [l_\alpha A]$ and $2\pi \nu [r\partial_r u_x]_{R_{N_r+\frac{1}{2}}}$ is impossible. We propose the multiring model (23) to overcome those difficulties. Indeed, by integrating over concentric rings of fluid the axisymmetric RNS-P equations (1) coupled to the elastic pressure law (18), we have derived a quasi-analytic radial discretization of the RNS-P equations (1). The resulting multiring system of equations can compute the velocity profile and therefore does not depend on unknown coefficients like all 1D models. It is a system of balance laws, where the left hand side is written as a system of conservation laws and the right hand side contains the mass, viscous and geometrical and mechanical source terms. This mathematical structure guarantees the conservation of mass and the balance of axial momentum and is conductive to a *finite volume* axial discretization. Next, we study the mathematical properties of this system of balance laws.

3. Mathematical properties

We study here the mathematical properties of both the single layer system of equations (10) and the multiring system of equations (23).

3.1. Single layer system of equations

We consider the homogeneous form of the single layer system of equations (10):

$$
\begin{cases}
\dfrac{\partial A_\alpha}{\partial t} + \dfrac{\partial Q_\alpha}{\partial x} = 0 & \text{(35a)} \\[2ex]
\dfrac{\partial Q_\alpha}{\partial t} + \dfrac{\partial F_{Q_\alpha}}{\partial x} = 0. & \text{(35b)}
\end{cases}
$$

This conservative system has been thoroughly studied by many authors and we only briefly recall its properties. Additional details can be found in [28,30,41].

The Jacobian matrix of system (35) has two real eigenvalues $\lambda_{1,\alpha}$ and $\lambda_{2,\alpha}$, respectively associated to two right eigenvectors $\boldsymbol{R_{1,\alpha}}$ and $\boldsymbol{R_{2,\alpha}}$:

$$
\lambda_{1,\alpha} = \frac{Q_\alpha}{A_\alpha} - c, \; \lambda_{2,\alpha} = \frac{Q_\alpha}{A_\alpha} + c \quad \text{and} \quad \boldsymbol{R_{1,\alpha}} = \begin{bmatrix} 1 \\ \lambda_{1,\alpha} \end{bmatrix}, \; \boldsymbol{R_{2,\alpha}} = \begin{bmatrix} 1 \\ \lambda_{2,\alpha} \end{bmatrix}, \tag{36}
$$

where c is the Moens–Korteweg celerity [42,43] and corresponds to the celerity of the elastic pulse waves propagating in the artery:

$$
c = \sqrt{\frac{K}{2\rho}\sqrt{A}}. \tag{37}
$$

The hyperbolicity of system (35) is characterized by the Shapiro number $S_{h,\alpha}$, introduced by Shapiro in [44]:

$$
S_{h,\alpha} = \frac{u_\alpha}{c}. \tag{38}
$$

The Shapiro number $S_{h,\alpha}$ is the analog of the Froude number F_r for the shallow water equations or of the Mach number Ma for compressible flows. Depending on the value of $S_{h,\alpha}$, we distinguish two flow regimes in the ring α: if $S_{h,\alpha} < 1$, the flow is subcritical and if $S_{h,\alpha} > 1$ the flow is supercritical. In both cases, system (35) is strictly hyperbolic as $\lambda_{1,\alpha} \neq \lambda_{2,\alpha}$ and the right eigenvectors $\boldsymbol{R_{1,\alpha}}$ and $\boldsymbol{R_{2,\alpha}}$ are linearly independent. In physiological conditions, blood flow is almost always subcritical [45,41], and therefore we only consider the case $S_{h,\alpha} < 1$.

The Riemann invariant vector $\boldsymbol{W_\alpha}$ associated with the system (35) is:

$$
\boldsymbol{W_\alpha} = \begin{bmatrix} W_{1,\alpha} \\ W_{2,\alpha} \end{bmatrix} = \begin{bmatrix} \dfrac{Q_\alpha}{A_\alpha} - 4c \\[2ex] \dfrac{Q_\alpha}{A_\alpha} + 4c \end{bmatrix}. \tag{39}
$$

The vector $\boldsymbol{W_\alpha}$ is linked to the conservative variables through the following relations:

$$
\begin{cases}
A_\alpha = \left(\dfrac{2\rho}{K}\right)^2 \left(\dfrac{W_{2,\alpha} - W_{1,\alpha}}{8}\right)^4 \\[3ex]
Q_\alpha = A_\alpha \dfrac{W_{1,\alpha} + W_{2,\alpha}}{2}.
\end{cases} \tag{40}
$$

The relations (40) are useful when defining boundary conditions at the inlet and outlet of the computational domain.

3.2. Two layers system of equations

We now focus on the more complicated inviscid two layers system of equations:

$$
\begin{cases}
\dfrac{\partial A}{\partial t} + \dfrac{\partial F_A}{\partial x} = 0 & \text{(41a)} \\[2ex]
\dfrac{\partial Q_1}{\partial t} + \dfrac{\partial F_{Q_1}}{\partial x} = S_{M,1} & \text{(41b)} \\[2ex]
\dfrac{\partial Q_2}{\partial t} + \dfrac{\partial F_{Q_2}}{\partial x} = S_{M,2}. & \text{(41c)}
\end{cases}
$$

To simplify the analysis, we suppose that the geometrical and mechanical properties of the artery do not vary ($S_T = 0$). In this case, system (41) can be written in the following quasi-linear form:

$$\boldsymbol{M}\frac{\partial \boldsymbol{X}}{\partial t} + \boldsymbol{H}\frac{\partial \boldsymbol{X}}{\partial x} = 0. \tag{42}$$

The vector $\boldsymbol{X}$ and the matrices $\boldsymbol{M}$ and $\boldsymbol{H}$ are respectively defined as:

$$\boldsymbol{X} = \begin{bmatrix} A \\ \bar{Q}_1 \\ \bar{Q}_2 \end{bmatrix}, \quad \boldsymbol{M} = \begin{bmatrix} 1 & 0 & 0 \\ -u & 1 & 0 \\ -u & 0 & 1 \end{bmatrix}, \quad \boldsymbol{H} = \begin{bmatrix} 0 & l & 1-l \\ c^2 - \frac{\bar{Q}_1^2}{A^2} & 2\frac{\bar{Q}_1}{A} - u & 0 \\ c^2 - \frac{\bar{Q}_2^2}{A^2} & 0 & 2\frac{\bar{Q}_2}{A} - u \end{bmatrix}, \tag{43}$$

where $l = l_{\frac{3}{2}}$, $u = u_{x,\frac{3}{2}}$, $Q_1 = l\bar{Q}_1$ and $Q_2 = (1-l)\bar{Q}_2$. System (42) is identical to the quasi-linear strictly hyperbolic system obtained in [38] for the two layers shallow water model with mass exchange. Therefore, the two layers system (41) is also strictly hyperbolic.

3.3. Multiring system of equations

In [38], the authors have studied the hyperbolicity of the multilayer shallow water system with mass exchange. They performed numerous numerical tests showing that for a given number of layers, the multilayer system is hyperbolic when small shear flows are considered. In regions of high shear, some eigenvalues can become complex and lead to the development of an Kelvin–Helmholtz-like instability [46]. This behavior is expected as the RNS-P equations (1) are not a system of conservation laws. By analogy, this analysis is valid for the multiring system of equation (23) and we assume that in physiological conditions the multiring system (23) is hyperbolic.

4. Numerical methods

For simplicity, we rewrite the multiring system of equations (23) in the following vectorial form:

$$\frac{\partial \boldsymbol{U}}{\partial t} + \frac{\partial \boldsymbol{F}}{\partial x} = \boldsymbol{S_M} + \boldsymbol{S_v} + \boldsymbol{S_T}, \tag{44}$$

where:

$$\boldsymbol{U} = \begin{bmatrix} A \\ Q_1 \\ \vdots \\ Q_{N_r} \end{bmatrix} \quad \text{and} \quad \boldsymbol{F} = \begin{bmatrix} F_A \\ F_{Q_1} \\ \vdots \\ F_{Q_{N_r}} \end{bmatrix}, \tag{45}$$

and:

$$\boldsymbol{S_M} = \begin{bmatrix} 0 \\ S_{M,1} \\ \vdots \\ S_{M,N_r} \end{bmatrix} \quad \text{and} \quad \boldsymbol{S_v} = \begin{bmatrix} 0 \\ S_{v,1} \\ \vdots \\ S_{v,N_r} \end{bmatrix} \quad \text{and} \quad \boldsymbol{S_T} = S_T \begin{bmatrix} 0 \\ l_1 \\ \vdots \\ l_{N_r} \end{bmatrix}. \tag{46}$$

The structure of the multiring system of equation (44) as a system of balance laws naturally leads us to propose a *finite volume* numerical scheme to obtain an approximate solution. Doing so, we ensure that the numerical scheme is robust, conservative and shock-capturing and that the numerical solution is positive if the chosen numerical flux preserves the positivity of the solution.

4.1. Problem splitting

The first step towards obtaining a numerical approximation of the solution of the multiring system of equations (44) in a *finite volume* framework is to discretize both the temporal and spatial domains. We first divide the time domain using a constant time step Δt and the discrete times are defined as:

$$t^n = n\Delta t \quad \text{for} \quad n \in \mathbb{N}. \tag{47}$$

We note $\boldsymbol{U^n} = \boldsymbol{U}(t^n)$. We then introduce a mesh in the axial direction and divide the length L of the artery in a series of cells C_i defined as:

$$C_i = \left[x_{i-\frac{1}{2}}, x_{i+\frac{1}{2}}\right] = [(i-1)\Delta x, i\Delta x] \quad \text{for} \quad i = 1, \dots, N_x, \tag{48}$$

where Δx is the cell size, supposed constant for simplicity, and $L = N_x \Delta x$. Finally, we discretize the multiring system of equations (44) using the following time splitting method:

$$
\begin{cases}
\dfrac{\boldsymbol{U}^* - \boldsymbol{U}^n}{\Delta t} + \dfrac{\partial}{\partial x} \left[\boldsymbol{F} \left(\boldsymbol{U}^n \right) \right] = \boldsymbol{S}_M \left(\boldsymbol{U}^n \right) + \boldsymbol{S}_T \left(\boldsymbol{U}^n \right) & \text{(49a)} \\[3mm]
\dfrac{\boldsymbol{U}^{n+1} - \boldsymbol{U}^*}{\Delta t} = \boldsymbol{S}_v \left(\boldsymbol{U}^{n+1} \right). & \text{(49b)}
\end{cases}
$$

Both the convective and viscous systems of equations (resp. eq. (49a) and (49b)) are solved numerically in the following subsections.

4.2. Explicit convective numerical scheme

We first solve the convective system of equations (49a) using an explicit *finite volume* scheme, which includes the mass exchange source term $\boldsymbol{S}_M$ and the geometrical and mechanical source term $\boldsymbol{S}_T$.

Integrating system (49a) over the cell C_i, we obtain the explicit *finite volume* scheme:

$$
\frac{\boldsymbol{U}_i^* - \boldsymbol{U}_i^n}{\Delta t} + \frac{1}{\Delta x} \left[\boldsymbol{F}_{i+\frac{1}{2}}^n - \boldsymbol{F}_{i-\frac{1}{2}}^n \right] = \boldsymbol{S}_{M,i}^n + \boldsymbol{S}_{T,i}^n, \tag{50}
$$

where $\boldsymbol{U}_i^n$ is the space-average approximation of the vector $\boldsymbol{U}$ in the cell C_i at the time t^n:

$$
\boldsymbol{U}_i^n \approx \frac{1}{\Delta x} \int_{C_i} \boldsymbol{U} \left(x, t^n \right) \mathrm{d}x. \tag{51}
$$

The vector $\boldsymbol{F}_{i+\frac{1}{2}}^n$ is the two-points numerical flux vector, and corresponds to the numerical approximation of the flux vector $\boldsymbol{F}$ at interface $x_{i+\frac{1}{2}}$ of the cell C_i at time t^n:

$$
\boldsymbol{F}_{i+\frac{1}{2}}^n = \mathcal{F} \left(\boldsymbol{U}_{i+\frac{1}{2},L}^n, \boldsymbol{U}_{i+\frac{1}{2},R}^n \right) =
\begin{bmatrix}
\mathcal{F}_A \left(\boldsymbol{U}_{i+\frac{1}{2},L}^n, \boldsymbol{U}_{i+\frac{1}{2},R}^n \right) \\[2mm]
\mathcal{F}_{Q_1} \left(\boldsymbol{U}_{i+\frac{1}{2},L}^n, \boldsymbol{U}_{i+\frac{1}{2},R}^n \right) \\
\vdots \\
\mathcal{F}_{Q_{N_r}} \left(\boldsymbol{U}_{i+\frac{1}{2},L}^n, \boldsymbol{U}_{i+\frac{1}{2},R}^n \right)
\end{bmatrix}. \tag{52}
$$

The flux $\mathcal{F}_A \left(\boldsymbol{U}_{i+\frac{1}{2},L}^n, \boldsymbol{U}_{i+\frac{1}{2},R}^n \right)$ can also be written as the sum of the contribution of each ring α:

$$
\mathcal{F}_A \left(\boldsymbol{U}_{i+\frac{1}{2},L}^n, \boldsymbol{U}_{i+\frac{1}{2},R}^n \right) = \sum_{j=1}^{N_r} \mathcal{F}_{A_j} \left(\boldsymbol{U}_{i+\frac{1}{2},L}^n, \boldsymbol{U}_{i+\frac{1}{2},R}^n \right) \tag{53}
$$

The choice of the vector function $\mathcal{F}$ defines the numerical flux and thus the *finite volume* scheme. As we use only a first-order *finite volume* numerical scheme, the vectors $\boldsymbol{U}_{i+\frac{1}{2},L}^n$ and $\boldsymbol{U}_{i+\frac{1}{2},R}^n$ at the left and right of the interface $x_{i+\frac{1}{2}}$ of the cell C_i at time t^n are defined as:

$$
\boldsymbol{U}_{i+\frac{1}{2},L}^n = \boldsymbol{U}_i^n \quad \text{and} \quad \boldsymbol{U}_{i+\frac{1}{2},R}^n = \boldsymbol{U}_{i+1}^n. \tag{54}
$$

The vectors $\boldsymbol{S}_{M,i}^n$ and $\boldsymbol{S}_{T,i}^n$ correspond respectively to the discretization of the mass exchange source term $\boldsymbol{S}_M \left(\boldsymbol{U}_i^n \right)$ and the geometrical and mechanical source term $\boldsymbol{S}_T \left(\boldsymbol{U}_i^n \right)$ and are specified in the following subsections.

4.2.1. Kinetic flux

As shown previously, there is no analytic expression for the eigenvalues of jacobian of the multiring system of equations (44). We therefore choose to use a kinetic flux function, which does not require the computation of the eigenstructure of system (44). Other approaches are possible, see [47,46]. A review of the kinetic method applied to different systems of equations can be found in [48] and more particularly to the 1D blood flow system in [19,41] and to the multilayer shallow water system with mass exchange in [38]. In the following, we briefly present the derivation of the expression of the kinetic vector function $\mathcal{F}$ for the multiring system of equations (44).

According to kinetic theory, the vector function $\mathcal{F}$ is defined as:

$$\mathcal{F}(U_L, U_R) = \mathcal{F}^+(U_L) + \mathcal{F}^-(U_R),$$ (55)

and $\mathcal{F}^+$ and $\mathcal{F}^-$ write:

$$\mathcal{F}^+ = \begin{bmatrix} \sum_{j=1}^{N_r} \mathcal{F}_{A_j}^+ \\ \mathcal{F}_{Q_1}^+ \\ \vdots \\ \mathcal{F}_{Q_{N_r}}^+ \end{bmatrix} \quad \text{and} \quad \mathcal{F}^- = \begin{bmatrix} \sum_{j=1}^{N_r} \mathcal{F}_{A_j}^- \\ \mathcal{F}_{Q_1}^- \\ \vdots \\ \mathcal{F}_{Q_{N_r}}^- \end{bmatrix}.$$ (56)

The fluxes $\mathcal{F}_{A_\alpha}^{\pm}$ and $\mathcal{F}_{Q_\alpha}^{\pm}$ in each ring α are defined as:

$$\begin{cases} \begin{bmatrix} \mathcal{F}_{A_\alpha}^+ \\ \mathcal{F}_{Q_\alpha}^+ \end{bmatrix} = \int\limits_{\xi \geq 0} \xi \begin{bmatrix} 1 \\ \xi \end{bmatrix} M_\alpha(A, \xi - u_\alpha)\, \mathrm{d}\xi \\ \begin{bmatrix} \mathcal{F}_{A_\alpha}^- \\ \mathcal{F}_{Q_\alpha}^- \end{bmatrix} = \int\limits_{\xi \leq 0} \xi \begin{bmatrix} 1 \\ \xi \end{bmatrix} M_\alpha(A, \xi - u_\alpha)\, \mathrm{d}\xi. \end{cases}$$ (57)

The function M_α is the kinetic Maxwellian, or so-called *Gibbs equilibrium*, and represents a distribution function of the microscopic particle velocity $\xi \in \mathbb{R}$ in the ring α:

$$M_\alpha(A, \xi - u_\alpha) = \frac{l_\alpha A}{\tilde{c}} \chi\left(\frac{\xi - u_\alpha}{\tilde{c}}\right),$$ (58)

where:

$$\tilde{c} = \sqrt{\frac{K}{3\rho}\sqrt{A}}.$$ (59)

We choose the function χ as:

$$\chi(w) = \begin{cases} \dfrac{1}{2\sqrt{3}} & \text{if } |w| \leq \sqrt{3} \\ 0 & \text{else.} \end{cases}$$ (60)

Injecting the expressions of the functions χ and M_α in the definition of the fluxes (57), we obtain after some computation the expressions for the fluxes $\mathcal{F}_{A_\alpha}^{\pm}$ and $\mathcal{F}_{Q_\alpha}^{\pm}$ in each ring α:

$$\begin{cases} \begin{bmatrix} \mathcal{F}_{A_\alpha}^+ \\ \mathcal{F}_{Q_\alpha}^+ \end{bmatrix} = \frac{l_\alpha A}{2\sqrt{3}\tilde{c}} \begin{bmatrix} \frac{1}{2}\left((\xi_{p,\alpha}^+)^2 - (\xi_{m,\alpha}^+)^2\right) \\ \frac{1}{3}\left((\xi_{p,\alpha}^+)^3 - (\xi_{m,\alpha}^+)^3\right) \end{bmatrix} \\ \begin{bmatrix} \mathcal{F}_{A_\alpha}^- \\ \mathcal{F}_{Q_\alpha}^- \end{bmatrix} = \frac{l_\alpha A}{2\sqrt{3}\tilde{c}} \begin{bmatrix} \frac{1}{2}\left((\xi_{p,\alpha}^-)^2 - (\xi_{m,\alpha}^-)^2\right) \\ \frac{1}{3}\left((\xi_{p,\alpha}^-)^3 - (\xi_{m,\alpha}^-)^3\right) \end{bmatrix}, \end{cases}$$ (61)

with:

$$\begin{cases} \xi_{p,\alpha}^+ = \max\left(0, u_\alpha + \sqrt{3}\tilde{c}\right), \quad \xi_{m,\alpha}^+ = \max\left(0, u_\alpha - \sqrt{3}\tilde{c}\right) \\ \xi_{p,\alpha}^- = \min\left(0, u_\alpha + \sqrt{3}\tilde{c}\right), \quad \xi_{m,\alpha}^- = \min\left(0, u_\alpha - \sqrt{3}\tilde{c}\right). \end{cases}$$ (62)

4.2.2. Mass exchange source term

We define the discrete mass exchange source term $S_{M,i}^n$ as:

$$
\boldsymbol{S}_{M,i}^n = \begin{bmatrix} 0 \\ u_{\frac{3}{2},i}^n G_{\frac{3}{2},i}^n \\ \vdots \\ u_{\alpha+\frac{1}{2},i}^n G_{\alpha+\frac{1}{2},i}^n - u_{\alpha-\frac{1}{2},i}^n G_{\alpha-\frac{1}{2},i}^n \\ \vdots \\ -u_{N_r-\frac{1}{2},i}^n G_{N_r-\frac{1}{2},i}^n \end{bmatrix} .
\tag{63}
$$

Following [38] and by analogy with expression (26), we compute $G_{\alpha+\frac{1}{2},i}^n$ in each ring α as:

$$
G_{\alpha+\frac{1}{2},i}^n = \frac{1}{\Delta x} \sum_{j=1}^{\alpha} \left\{ \left[\mathcal{F}_{A_j}\left(\boldsymbol{U}_{i+\frac{1}{2},L}^n, \boldsymbol{U}_{i+\frac{1}{2},R}^n \right) - \mathcal{F}_{A_j}\left(\boldsymbol{U}_{i-\frac{1}{2},L}^n, \boldsymbol{U}_{i-\frac{1}{2},R}^n \right) \right] - \right.
$$
$$
\left. l_j \left[\mathcal{F}_A\left(\boldsymbol{U}_{i+\frac{1}{2},L}^n, \boldsymbol{U}_{i+\frac{1}{2},R}^n \right) - \mathcal{F}_A\left(\boldsymbol{U}_{i-\frac{1}{2},L}^n, \boldsymbol{U}_{i-\frac{1}{2},R}^n \right) \right] \right\} .
\tag{64}
$$

We define $u_{\alpha+\frac{1}{2},i}^n$ in an upwind manner:

$$
u_{\alpha+\frac{1}{2},i}^n = \begin{cases} u_{\alpha,i}^n & \text{if} \quad G_{\alpha+\frac{1}{2},i}^n \leq 0 \\ u_{\alpha+1,i}^n & \text{if} \quad G_{\alpha+\frac{1}{2},i}^n > 0. \end{cases}
\tag{65}
$$

This choice is motivated by the analysis of expression (11) for the mass exchange term $G_{\alpha+\frac{1}{2}}$. Indeed, $G_{\alpha+\frac{1}{2}} > 0$ if the cross-sectional area $\pi R_{\alpha+\frac{1}{2}}^2$ increases with time or if the interface velocity $u_{r,\alpha+\frac{1}{2}} < 0$. In both cases, from the perspective of the interface $R_{\alpha+\frac{1}{2}}$, the flow is coming from the upper ring $\alpha+1$ and the upwind velocity is therefore $u_{x,\alpha+1}$.

4.2.3. Hydrostatic reconstruction

The considered kinetic flux function does not take into account the geometrical and mechanical source term $\boldsymbol{S}_T$, which results from axial variations of the neutral cross-sectional area A_0 or the arterial rigidity K. This source term must be treated using a well-balanced method to prevent spurious oscillations of the numerical solution close to steady states [49–52]. To that effect, we use the well-balanced hydrostatic reconstruction technique (HR for short) introduced in [53] for shallow water equations. This technique was then applied to blood flow equations in [54,55,41] and to the multilayer shallow water system with mass exchange in [38]. Through a reconstruction of the conservative variables, HR allows to obtain a simple and efficient well-balanced numerical scheme given any *finite volume* numerical flux. Next, we briefly recall the derivation of HR applied to the multiring system of equations (44).

We define the discrete geometrical and mechanical source term $\boldsymbol{S}_{T,i}^n$ as:

$$
\boldsymbol{S}_{T,i}^n = S_{T,i}^n \begin{bmatrix} 0 \\ l_1 \\ \vdots \\ l_{N_r} \end{bmatrix} ,
\tag{66}
$$

where $S_{T,i}^n$ is:

$$
S_{T,i}^n = \frac{1}{3\rho\Delta x} \left[K_{i+\frac{1}{2}}^* \left[A_{i+\frac{1}{2},L}^{*n} \right]^{\frac{3}{2}} - K_{i+\frac{1}{2},L} \left[A_{i+\frac{1}{2},L}^n \right]^{\frac{3}{2}} - K_{i-\frac{1}{2}}^* \left[A_{i-\frac{1}{2},R}^{*n} \right]^{\frac{3}{2}} + K_{i-\frac{1}{2},R} \left[A_{i-\frac{1}{2},R}^n \right]^{\frac{3}{2}} \right] .
\tag{67}
$$

The reconstructed variables $A_{i+\frac{1}{2},L}^{*n}$, $A_{i+\frac{1}{2},R}^{*n}$ and $K_{i+\frac{1}{2}}^*$ are defined such that the steady states at rest are preserved as well as the positivity of the cross-sectional area A:

$$
\begin{cases} A_{i+\frac{1}{2},L}^{*n} = \left[\dfrac{H_{i+\frac{1}{2},L}^{*n}}{K_{i+\frac{1}{2}}^*} \right]^2 \\[3ex] A_{i+\frac{1}{2},R}^{*n} = \left[\dfrac{H_{i+\frac{1}{2},R}^{*n}}{K_{i+\frac{1}{2}}^*} \right]^2 \\[3ex] K_{i+\frac{1}{2}}^* = \max\left(K_{i+\frac{1}{2},L}, K_{i+\frac{1}{2},R} \right), \end{cases}
\tag{68}
$$

with:

$$
\begin{cases}
H^{*n}_{i+\frac{1}{2},L} = \max\left(0, Z^*_{i+\frac{1}{2}} + \left[K\sqrt{A}\right]_{i+\frac{1}{2},L} - \left[K\sqrt{A_0}\right]_{i+\frac{1}{2},L}\right)\\[6pt]
H^{*n}_{i+\frac{1}{2},R} = \max\left(0, Z^*_{i+\frac{1}{2}} + \left[K\sqrt{A}\right]_{i+\frac{1}{2},R} - \left[K\sqrt{A_0}\right]_{i+\frac{1}{2},R}\right)\\[6pt]
Z^*_{i+\frac{1}{2}} = \min\left(\left[K\sqrt{A_0}\right]_{i+\frac{1}{2},L}, \left[K\sqrt{A_0}\right]_{i+\frac{1}{2},R}\right).
\end{cases}
\tag{69}
$$

Finally, we obtain a well-balanced numerical scheme by replacing each occurrence of the conservative vectors $\boldsymbol{U}^n_{i+\frac{1}{2},L}$ and $\boldsymbol{U}^n_{i+\frac{1}{2},R}$ in the vector function $\mathcal{F}$ by the reconstructed conservative vectors $\boldsymbol{U}^{*n}_{i+\frac{1}{2},L}$ and $\boldsymbol{U}^{*n}_{i+\frac{1}{2},R}$, defined as:

$$
\boldsymbol{U}^{*n}_{i+\frac{1}{2},L} = \begin{bmatrix} A^{*n}_{i+\frac{1}{2},L}\\ Q^n_{1,i+\frac{1}{2},L}\\ \vdots\\ Q^n_{N_r,i+\frac{1}{2},L} \end{bmatrix}, \quad
\boldsymbol{U}^{*n}_{i+\frac{1}{2},R} = \begin{bmatrix} A^{*n}_{i+\frac{1}{2},R}\\ Q^n_{1,i+\frac{1}{2},R}\\ \vdots\\ Q^n_{N_r,i+\frac{1}{2},R} \end{bmatrix}.
\tag{70}
$$

4.2.4. CFL condition

The stability of the convective numerical scheme is ensured if at each time t_n, the time step Δt verifies the following CFL (Courant, Friedrichs and Lewy) [56] condition:

$$
\Delta t \le \min_{i=1}^{N_x} \min_{j=1}^{N_r} \frac{l_j A^n_i \Delta x}{l_j A^n_i \left(|u^n_{j,i}| + \tilde{c}^n_i\right) + \Delta x \left(G^n_{j+\frac{1}{2},i} - G^n_{j-\frac{1}{2},i}\right)}.
\tag{71}
$$

This CFL condition ensures that the kinetic scheme preserves the positivity of the cross-sectional area A (for a detailed proof see [38]). Note that its more restrictive than the classical CFL condition used in 1D blood flow models as the flow can now exit the ring through both its axial and radial interfaces.

4.3. Implicit viscous numerical scheme

We solve the viscous system of equations (49b) using an implicit numerical scheme, chosen for stability reasons.

Integrating system (49b) over the cell C_i, we obtain the following implicit viscous numerical scheme:

$$
\frac{\boldsymbol{U}^{n+1}_i - \boldsymbol{U}^*_i}{\Delta t} = \boldsymbol{S}^{n+1}_{v,i},
\tag{72}
$$

where $\boldsymbol{U}^*_i$ is the solution of the convective numerical scheme (50) in the cells C_i and $\boldsymbol{S}^{n+1}_{v,i}$ is the discretization of the viscous source term $\boldsymbol{S}_v\left(\boldsymbol{U}^{n+1}_i\right)$ and writes:

$$
\boldsymbol{S}^{n+1}_{v,i} = \begin{bmatrix} 0\\ S^{n+1}_{v,1,i}\\ \vdots\\ S^{n+1}_{v,N_r,i} \end{bmatrix}.
\tag{73}
$$

In each ring α of the cell C_i at time t^{n+1}, we define $S^{n+1}_{v,\alpha,i}$ as the discrete analog of $S_{v,\alpha}$ (13). To compute $S^{n+1}_{v,\alpha,i}$, we use a centered *finite difference* discretization of the term $\left[r\frac{\partial u_x}{\partial r}\right]_{R_{\alpha+\frac{1}{2}}}$, which writes:

$$
\left[r\frac{\partial u_x}{\partial r}\right]_{R_{\alpha+\frac{1}{2}}} = J_{r,\alpha}\left[u^{n+1}_{\alpha+1,i} - u^{n+1}_{\alpha,i}\right] \quad \text{for} \quad \alpha = 1,\ldots,N_r - 1,
\tag{74}
$$

where:

$$
J_{r,\alpha} = 2\frac{\sum_{j=1}^{\alpha} l_{r,j}}{l_{r,\alpha} + l_{r,\alpha+1}}.
\tag{75}
$$

At the interfaces $R_{\frac{1}{2}}$ and $R_{N_r+\frac{1}{2}}$, the previous discretization (74) of $\left[r\frac{\partial u_x}{\partial r}\right]$ is not possible and the boundary conditions (19) and (21) must be taken into account. At the ring interface $R_{\frac{1}{2}}$, the axisymmetric boundary condition (19) imposes that:

$$\left[r\frac{\partial u_x}{\partial r}\right]_{R_{\frac{1}{2}}} = 0. \tag{76}$$

To express $\left[r\frac{\partial u_x}{\partial r}\right]_{R_{N_r+\frac{1}{2}}}$ at the ring interface $R_{N_r+\frac{1}{2}}$ using only the conservative vector $\boldsymbol{U}$, we first perform the following asymptotic expansion of u_x in the ring N_r:

$$u_x = u_{x,N_r+\frac{1}{2}} + \left[r - R_{N_r+\frac{1}{2}}\right]\frac{\partial u_x}{\partial r}\Big|_{R_{N_r+\frac{1}{2}}} + O\left(\left[R_{N_r+\frac{1}{2}} - r\right]^2\right). \tag{77}$$

Neglecting the higher-order terms and using the no-slip boundary condition (21), we obtain the following expression:

$$u_x \approx \left[r - R_{N_r+\frac{1}{2}}\right]\frac{\partial u_x}{\partial r}\Big|_{R_{N_r+\frac{1}{2}}}. \tag{78}$$

We then integrate this expression over the cross-sectional area of the ring N_r and we obtain:

$$\left[r\frac{\partial u_x}{\partial r}\right]_{R_{N_r+\frac{1}{2}}} = J_{r,\nu}\frac{Q_{N_r,i}^{n+1}}{A_i^{n+1}}, \tag{79}$$

with:

$$J_{r,\nu} = \frac{1}{-\frac{1}{3} + \left[1 - l_{r,N_r}\right]^2 - \frac{2}{3}\left[1 - l_{r,N_r}\right]^3}. \tag{80}$$

It is important to note that the discretization (79) of $\left[r\frac{\partial u_x}{\partial r}\right]_{R_{N_r+\frac{1}{2}}}$ imposes the no-slip boundary condition (21) at the wall, which is the natural boundary condition for viscous flows.

Finally, noticing that the first component of the source term $\boldsymbol{S_\nu}$ is zero, we obtain the following trivial solution of the system of equations (49b) for the first component of $\boldsymbol{U_i^{n+1}}$:

$$A_i^{n+1} = A_i^* \quad \text{for} \quad i = 1, \ldots, N_x. \tag{81}$$

We can therefore rewrite the implicit viscous scheme (72) in the following matrix form:

$$\left[\mathbb{I} + \Delta t\boldsymbol{M_{\nu,i}^*}\right]\begin{bmatrix} Q_{1,i}^{n+1} \\ \vdots \\ Q_{\alpha,i}^{n+1} \\ \vdots \\ Q_{N_r,i}^{n+1} \end{bmatrix} = \begin{bmatrix} Q_{1,i}^* \\ \vdots \\ Q_{\alpha,i}^* \\ \vdots \\ Q_{N_r,i}^* \end{bmatrix}, \tag{82}$$

where $\mathbb{I}$ is the identity matrix and $\boldsymbol{M_{\nu,i}^*}$ is the following tridiagonal matrix:

$$\boldsymbol{M_{\nu,i}^*} = \frac{2\pi\nu}{A_i^*}\begin{bmatrix} \frac{J_{r,1}}{l_1} & -\frac{J_{r,1}}{l_2} & 0 & \cdots & 0 \\ \ddots & \ddots & \ddots & \ddots & \vdots \\ 0 & -\frac{J_{r,\alpha-1}}{l_{\alpha-1}} & \frac{J_{r,\alpha-1}+J_{r,\alpha}}{l_\alpha} & -\frac{J_{r,\alpha}}{l_{\alpha+1}} & 0 \\ \vdots & \ddots & \ddots & \ddots & \ddots \\ 0 & \cdots & 0 & -\frac{J_{r,N_r-1}}{l_{N_r-1}} & \frac{J_{r,N_r-1}}{l_{N_r}} - J_{r,\nu} \end{bmatrix}. \tag{83}$$

We invert system (82) using the Thomas algorithm [57], well-suited for solving tridiagonal matrix systems.

To conclude the description of the numerical scheme we use to solve the multiring system of equations (44), we provide in the following methodologies to impose inlet and outlet boundary conditions.

5. Boundary conditions

As we compute subcritical solutions of system (44), boundary conditions are required at both ends of the computational domain. We impose these boundary conditions in inlet and outlet ghost cells, respectively noted C_{in} and C_{out}. Therefore, in both ghost cells C_{in} and C_{out}, the corresponding vectors of conservative variables $\boldsymbol{U_{in}^n}$ and $\boldsymbol{U_{out}^n}$ must be prescribed in order to update the numerical solution from time t^n to time t^{n+1} in each cell C_i of the computational domain. We propose methodologies to impose these boundary conditions, but we describe only the derivation of the inlet boundary conditions as the implementation of inlet and outlet boundary conditions is very similar.

5.1. Imposed flow rate

We wish to impose the flow rate $Q_{e,\alpha}^n$ at the interface between the first cell C_1 and the inlet ghost cell C_{in} of each ring α, namely:

$$\mathcal{F}_{A_\alpha}\left(\boldsymbol{U_{in}^n}, \boldsymbol{U_1^n}\right) = Q_{e,\alpha}^n \quad \text{for} \quad \alpha = 1, \dots, N_r. \tag{84}$$

Following the methodology proposed in [58] and taking advantage of the fact that the kinetic flux function $\mathcal{F}_{A_\alpha}$ can be split in two, equation (84) rewrites as:

$$\mathcal{F}_{A_\alpha}^+\left(\boldsymbol{U_{in}^n}\right) + \mathcal{F}_{A_\alpha}^-\left(\boldsymbol{U_1^n}\right) = Q_{e,\alpha}^n \quad \text{for} \quad \alpha = 1, \dots, N_r. \tag{85}$$

To ensure the stability of the scheme, condition (85) is imposed in each ring α in an upwind manner. Consequently, we define the quantity:

$$\Delta Q = \sum_{\alpha=1}^{N_r} Q_{e,\alpha}^n - \mathcal{F}_{A_\alpha}^-\left(\boldsymbol{U_1^n}\right), \tag{86}$$

and distinguish two cases:

- If $\Delta Q \leq 0$, the dominant part of the information is coming from inside the computational domain. As we are performing an upwind evaluation of the inlet boundary condition, we impose:

$$\begin{cases} \mathcal{F}_A^+\left(\boldsymbol{U_{in}^n}\right) = 0 \\ \mathcal{F}_{Q_\alpha}^+\left(\boldsymbol{U_{in}^n}\right) = 0 \quad \text{for} \quad \alpha = 1, \dots, N_r. \end{cases} \tag{87}$$

- If $\Delta Q > 0$, the dominant part of the information is coming from outside the computational domain. In this case, we impose:

$$\begin{cases} \mathcal{F}_{A_\alpha}^+\left(\boldsymbol{U_{in}^n}\right) = Q_{e,\alpha}^n - \mathcal{F}_{A_\alpha}^-\left(\boldsymbol{U_1^n}\right) \quad \text{for} \quad \alpha = 1, \dots, N_r \\ W_1\left(\boldsymbol{U_{in}^n}\right) = W_1\left(\boldsymbol{U_1^n}\right). \end{cases} \tag{88}$$

The scalar function W_1 is the 1D analog of the Riemann invariant $W_{1,\alpha}$ in the ring α and characterizes the global outgoing characteristic. It writes:

$$W_1 = \frac{\sum_{\alpha=1}^{N_r} Q_\alpha}{A} - c. \tag{89}$$

Similarly, we write W_2 as:

$$W_2 = \frac{\sum_{\alpha=1}^{N_r} Q_\alpha}{A} + c. \tag{90}$$

We compute the inlet vector of conservative variables $\boldsymbol{U_{in}^n}$ in the ghost cell C_{in} by either solving system (87) or system (88). This can be done using a classic Newton's method in a limited number of iterations.

5.2. Imposed cross-sectional area

We wish to impose the cross-sectional area A_e^n in the inlet ghost cell C_{in}. Therefore, we set:

$$A_{in}^n = A_e^n. \tag{91}$$

To completely determine the inlet vector of conservative variables $\boldsymbol{U_{in}^n}$, we estimate the outgoing Riemann invariant $W_{1,\alpha}\left(\boldsymbol{U_{in}^n}\right)$ in the ring α as:

$$W_{1,\alpha}\left(\boldsymbol{U_{in}^n}\right) = W_{1,\alpha}\left(\boldsymbol{U_1^n}\right) \quad \text{for} \quad \alpha = 1, \ldots, N_r, \tag{92}$$

and using equations (39) and (40), we compute $W_{2,\alpha}\left(\boldsymbol{U_{in}^n}\right)$ and then $Q_{in,\alpha}^n$ in each ring α:

$$\begin{cases} W_{2,\alpha}\left(\boldsymbol{U_{in}^n}\right) = W_{1,\alpha}\left(\boldsymbol{U_{in}^n}\right) + 8c_{in}^n \\ Q_{in,\alpha}^n = l_\alpha A_{in}^n \dfrac{W_{1,\alpha}\left(\boldsymbol{U_{in}^n}\right) + W_{2,\alpha}\left(\boldsymbol{U_{in}^n}\right)}{2}. \end{cases} \tag{93}$$

5.3. Imposed reflection coefficient

We wish to impose the reflection coefficient R_t in the inlet ghost cell C_{in}. The inlet reflection coefficient R_t is defined as:

$$W_2\left(\boldsymbol{U_{in}^n}\right) - W_2\left(\boldsymbol{U_{in}^0}\right) = -R_t\left[W_1\left(\boldsymbol{U_{in}^n}\right) - W_1\left(\boldsymbol{U_{in}^0}\right)\right], \tag{94}$$

and characterizes the proportion of the outgoing information reflected back into the computational domain. When we wish to remove any reflection of the outgoing information, we set $R_t = 0$. We first estimate the outgoing Riemann invariant $W_1\left(\boldsymbol{U_{in}^n}\right)$ as:

$$W_1\left(\boldsymbol{U_{in}^n}\right) = W_1\left(\boldsymbol{U_1^n}\right), \tag{95}$$

and using equation (94), we compute $W_2\left(\boldsymbol{U_{in}^n}\right)$ and then A_{in}^n:

$$A_{in}^n = \left(\frac{2\rho}{K_{in}}\right)^2 \left(\frac{W_2\left(\boldsymbol{U_{in}^n}\right) - W_1\left(\boldsymbol{U_{in}^n}\right)}{8}\right)^4. \tag{96}$$

Finally, we use the methodology presented in the previous subsection to completely determine the inlet vector of conservative variables $\boldsymbol{U_{in}^n}$.

In the following sections, we perform a series of numerical tests to validate the multiring model (23), the numerical scheme and the boundary conditions previously described.

6. Linear examples in an elastic artery

6.1. The Womersley solution

In [22], Womersley proposed an analytic harmonic solution of the linearized Navier–Stokes equations which is also a solution of the linearized RNS-P equations (1). The Womersley solution is an important test case for numerical methods simulating blood flow in elastic arteries as it includes pulsatile effects, elastic deformation of the arterial wall and viscous dissipation. In [34,37,59], the authors used the Womersley solution in a rigid axisymmetric tube to validate their numerical method. In this section, we compute the Womersley solution in an elastic artery as a first validation case of the multiring model (23).

6.1.1. Linear harmonic solution
We first briefly detail the derivation of the Womersley solution starting from the linear RNS-P system of equations:

$$\begin{cases} \dfrac{1}{r}\dfrac{\partial}{\partial r}\left[ru_r\right] + \dfrac{\partial u_x}{\partial x} = 0 & \text{(97a)} \\[2ex] \dfrac{\partial u_x}{\partial t} = -\dfrac{1}{\rho}\dfrac{\partial p}{\partial x} + \dfrac{\nu}{r}\dfrac{\partial}{\partial r}\left[r\dfrac{\partial u_x}{\partial r}\right] & \text{(97b)} \\[2ex] p\left(x,r,t\right) = p\left(x,t\right). & \text{(97c)} \end{cases}$$

Following [22], we search for a harmonic solution of the axial velocity u_x, the pressure p and the radius R:

$$\begin{cases} u_x = \hat{u}_x(r)e^{i[\omega t - kx]} \\ p = p_0 + \hat{p}e^{i[\omega t - kx]} \\ R = R_0(x) + \hat{R}e^{i[\omega t - kx]}, \end{cases} \tag{98}$$

with $\hat{R} \ll 1$. For simplicity we choose $p_0 = 0$. Injecting the expressions (98) in the linear momentum equation (97b), we obtain:

$$\frac{\partial^2 \hat{u}_x}{\partial r^2} + \frac{1}{r} \frac{\partial \hat{u}_x}{\partial r} - i \frac{\alpha^2}{R^2} \hat{u}_x = -\frac{i\omega}{\mu c} \hat{p}, \tag{99}$$

where α is the Womersley number and c is the wave celerity, respectively defined as:

$$\alpha = R \sqrt{\frac{\omega}{\nu}} \quad \text{and} \quad c = \frac{\omega}{k}. \tag{100}$$

The Womersley number α represents the relative importance of pulsatile effects with respect to viscous effects and is the relevant dimensionless number in this example. Combining both the homogeneous solution of equation (99), computed using the Bessel function J_0, and the particular solution of equation (99), we obtain the general solution of equation (99), using the no-slip boundary condition at the wall (21):

$$\hat{u}_x = \frac{\hat{p}}{\rho c} \left[1 - \frac{J_0 \left(i^{\frac{3}{2}} \alpha \frac{r}{R} \right)}{J_0 \left(i^{\frac{3}{2}} \alpha \right)} \right]. \tag{101}$$

Using expression (101), we compute the flow rate Q and the wall shear stress (WSS) τ_w as:

$$Q = \hat{Q} e^{i[\omega t - kz]} \quad \text{with} \quad \hat{Q} = \int_0^{2\pi} \int_0^R \hat{u}_x r dr d\theta = \pi R^2 \frac{\hat{p}}{\rho c} [1 - F_{10}(\alpha)], \tag{102}$$

and:

$$\tau_w = \hat{\tau}_w e^{i[\omega t - kz]} \quad \text{with} \quad \hat{\tau}_w = -\mu \frac{\partial u_x}{\partial r} \bigg|_{r=R} = i \frac{\nu \alpha^2}{2R} \frac{\hat{p}}{\rho c} F_{10}(\alpha), \tag{103}$$

where F_{10} is defined as:

$$F_{10}(\alpha) = \frac{2}{i^{\frac{3}{2}} \alpha} \frac{J_1(i^{\frac{3}{2}} \alpha)}{J_0(i^{\frac{3}{2}} \alpha)}. \tag{104}$$

Finally, after integrating the incompressibility equation (97a) over the cross-sectional area of the artery, we obtain the following linearized expression for the wave celerity c:

$$c = \frac{\hat{p}}{\hat{R}} \frac{R_0}{2\rho} [1 - F_{10}(\alpha)]. \tag{105}$$

The inlet boundary condition imposes the value of either $\hat{p}$ or $\hat{R}$, which are linked through the elastic pressure law (18):

$$\frac{\hat{p}}{\hat{R}} = \sqrt{\pi} K. \tag{106}$$

Next, we compare the numerical solution of the multiring model (23) to the linear harmonic Womersley solution presented previously.

6.1.2. Numerical results

We consider a straight artery initially at rest:

$$\begin{cases} A(x, t = 0) = A_0 \\ Q_\alpha (x, t = 0) = 0 \quad \text{for} \quad \alpha = 1, \dots, N_r. \end{cases} \tag{107}$$

We impose at the inlet a sinusoidal oscillation of the pressure:

$$p(x = 0, t) = \hat{p} \sin \left(2\pi \frac{t}{T_c} \right) \quad \text{with} \quad \hat{p} = \sqrt{\pi} K \hat{R}, \tag{108}$$

and at the outlet a zero reflection coefficient R_t to remove any backward traveling waves. The values of the geometrical and mechanical parameters describing the artery as well as those describing the inlet and outlet boundary conditions are presented in Table 1 and are given in the "cgs" unit system. They mimic physiological conditions and the value of $\hat{R}$ is chosen small enough such that the linear approximation required to obtain the Womersley solution is valid. The final

Table 1
Elastic Womersley example – Geometrical and mechanical parameters describing the artery and the inlet and outlet boundary conditions, given in the "cgs" unit system.

L	R_0	K	ρ	μ	$\hat{R}$	R_t	T_c	t_f	α
200	1	10^4	1	$2\pi \frac{\rho}{T_c} \frac{R_0^2}{\alpha^2}$	10^{-3}	0	0.5	$12T_c$	$\{5, 20\}$
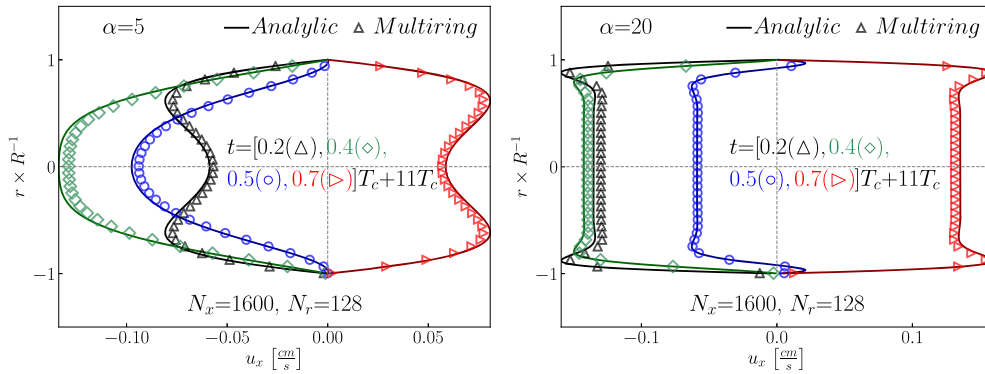
Fig. 2. Elastic Womersley example – Comparison between the analytic Womersley velocity profiles (——) and the computed multiring velocity profiles (marks) obtained using $N_x = 1600$ cells and $N_r = 128$ rings in $x = 25$ at times $t \in \{0.2\,(\triangle),\ 0.4\,(\diamond),\ 0.5\,(\circ),\ 0.7\,(\triangleright)\}T_c + 11T_c$ for $\alpha = 5$ (left) and $\alpha = 20$ (right). We observe that the multiring numerical solutions agree well with the analytic Womersley solutions.

simulation time t_f is chosen large enough to reach a periodic regime. For the sake of illustration, we consider only two different Womersley numbers, $\alpha = 5$ and $\alpha = 20$, selected to respectively represent flow conditions in arterioles and large arteries. At small Womersley numbers ($\alpha = 5$), viscous effects dominate, whereas at large Womersley numbers ($\alpha = 20$), unsteady advection effects are dominant.

In Fig. 2, we plot the analytic and multiring Womersley velocity profiles obtained in $x = 25$ at $t \in \{0.2, 0.4, 0.5, 0.7\}T_c + 11T_c$ for $\alpha = 5$ (Fig. 2 left) and $\alpha = 20$ (Fig. 2 right). We use $N_x = 1600$ cells and $N_r = 128$ rings. We observe that for both Womersley numbers $\alpha = 5$ and $\alpha = 20$, the analytic and multiring velocity profiles are well matched for each recorded time. Small discrepancies between both solutions appear near the maxima of velocity due to the numerical dissipation of the kinetic scheme and the small intrinsic nonlinearities of the multiring numerical solution.

In Fig. 3, we represent the spatial evolution of the flow rate Q, the pressure p and the wall shear stress (WSS) τ_w computed with the analytic Womersley solution and the multiring model at time $t = 0.3T_c + 11T_c$ for $\alpha = 5$ (Fig. 3 left) and $\alpha = 20$ (Fig. 3 right). Once again, we use $N_x = 1600$ cells and $N_r = 128$ rings. For $\alpha = 20$, the Womersley and the multiring solutions are superposed except at the local maxima and minima of Q, p and τ_w due to the numerical dissipation of the multiring numerical scheme. For $\alpha = 5$, both solutions match almost perfectly as in this case the viscous dissipation is much larger than the numerical dissipation.

Next, we perform a convergence analysis in both the number of cells N_x and the number of rings N_r. In Fig. 4, we plot the evolution of the L_2 spatial error between the analytic Womersley and the multiring numerical solutions with the dimensionless number of cells $\bar{N}_x = \lambda N_x / L$, where λ is the wavelength of the pressure pulse, and with the dimensionless number of rings $\bar{N}_r = N_r / \alpha$ for $\alpha = 5$ (Fig. 4 left) and $\alpha = 20$ (Fig. 4 right). We focus only on the flow rate Q and the WSS τ_w taken at time $t = 0.3T_c + 11T_c$. For both $\alpha = 5$ and $\alpha = 20$, we observe that increasing $\bar{N}_x$ or $\bar{N}_r$ is not equivalent. For low values of $\bar{N}_x$, increasing $\bar{N}_r$ does not significantly decrease the error, whereas increasing $\bar{N}_x$ does. On the contrary, for high values of $\bar{N}_x$, increasing $\bar{N}_r$ significantly decreases the error, whereas increasing $\bar{N}_x$ does not. This behavior is expected as wave propagation in the axial direction is the main physical behavior described by the Womersley solution and can only be captured if a sufficient number of cells $\bar{N}_x$ is used. Only then can we increase the number of rings $\bar{N}_r$ to compute in detail the velocity profile. However, the behavior of the WSS τ_w for $\alpha = 20$ is different from the behavior of the other quantities as the effect of increasing the number of rings $\bar{N}_r$ for low values of $\bar{N}_x$ is significant. This behavior can be explained by the fact that for $\alpha = 20$, the boundary layer near the wall is thin, therefore increasing $\bar{N}_r$ immediately allows to better capture the viscous behavior of the flow near the wall and therefore the WSS τ_w. As a rule of thumbs, we observe that $\bar{N}_x = 500$ and $\bar{N}_r = 2$ is the minimum mesh and ring refinements necessary to obtain an accurate description of the Womersley solution.

To conclude the analysis of the Womersley solution, we study three additional flow configurations where we increase the nonlinearity of the flow by changing the amplitude of the wall perturbation $\hat{R}$. We choose $\hat{R} \in \{10^{-3}, 10^{-2}, 10^{-1}, 3 \times 10^{-1}\}$. In Fig. 5, we plot snapshots of the spatial evolution of the axial velocity profile u_x computed with the multiring model at time $t = 0.3T_c + 11T_c$ for $\alpha = 20$ using $N_x = 1600$ cells and $N_r = 128$ rings. The values of the other geometrical and mechanical parameters describing the artery are identical to those presented in Table 1. We observe that the multiring
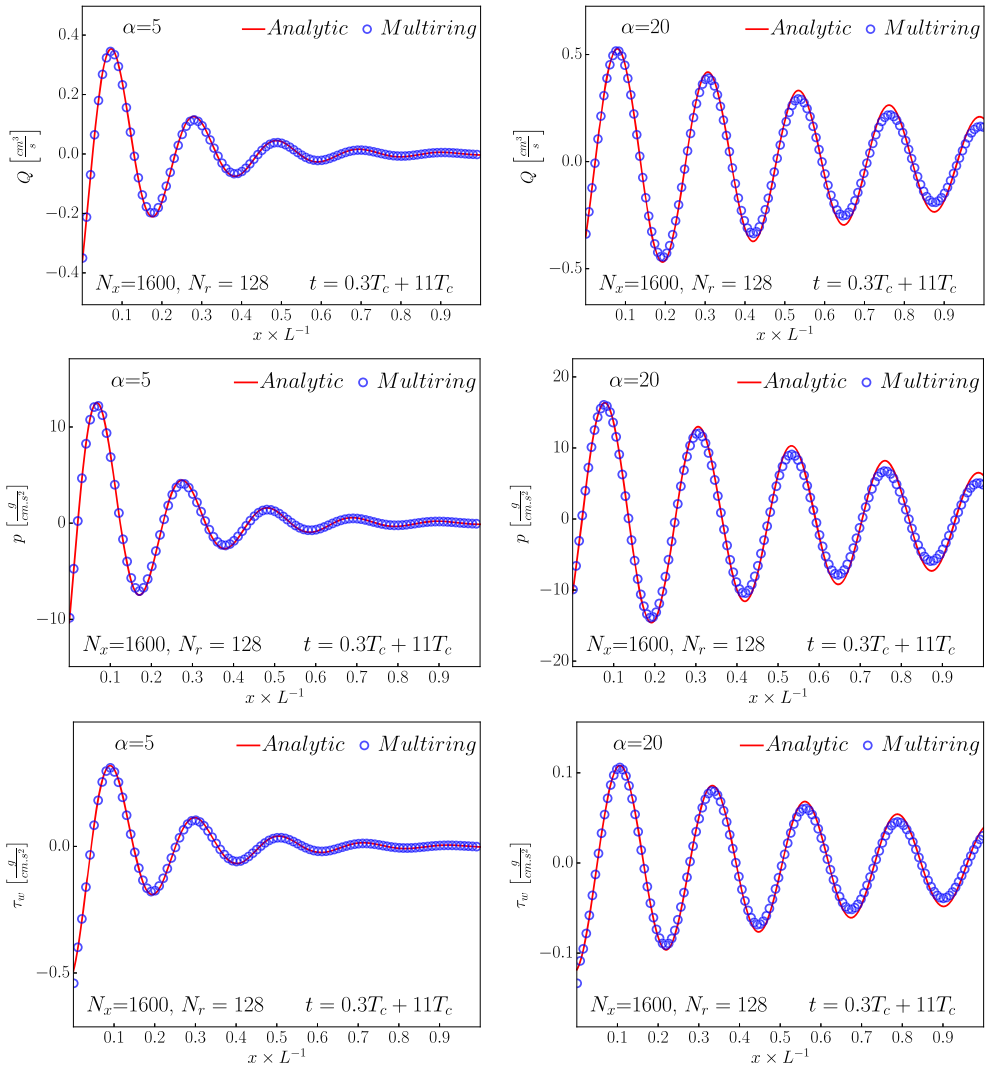
Fig. 3. Elastic Womersley example – Spatial evolution of the flow rate Q (top), the pressure p (middle) and the WSS τ_w (bottom) computed with the analytic Womersley solution (——) and with the multiring model (○) using $N_x = 1600$ cells and $N_r = 128$ rings at time $t = 0.3T_c + 11T_c$ for $\alpha = 5$ (left) and $\alpha = 20$ (right). We observe that the multiring solutions agree well with the analytic Womersley solutions.

model (23) is able to compute nonlinear flow behaviors with small and large deformations of the arterial wall without requiring any mesh adaptation strategy or particular numerical effort.

6.2. The steady linear elastic Poiseuille solution

In [60], Fung proposed a steady analytic solution of the linear RNS-P equations (97) in an elastic artery. As the Poiseuille solution, it describes the steady balance between the pressure gradient and the viscous radial dissipation term but takes into account the elastic deformation of the wall:

$$
\begin{cases}
u = \dfrac{2Q}{\pi R^2} \left[1 - \left[\dfrac{r}{R(x)} \right]^2 \right] \\[2ex]
p = p_0 + K\sqrt{\pi}\left[R - R_0\right] \\[2ex]
R = \left[R^5(x=0) - \dfrac{40\nu Q}{\pi^{\frac{3}{2}} K} x \right]^{\frac{1}{5}} \\[2ex]
Q = \dfrac{\pi^{\frac{3}{2}} K}{40\nu L} \left[R^5(x=0) - R^5(x=L) \right].
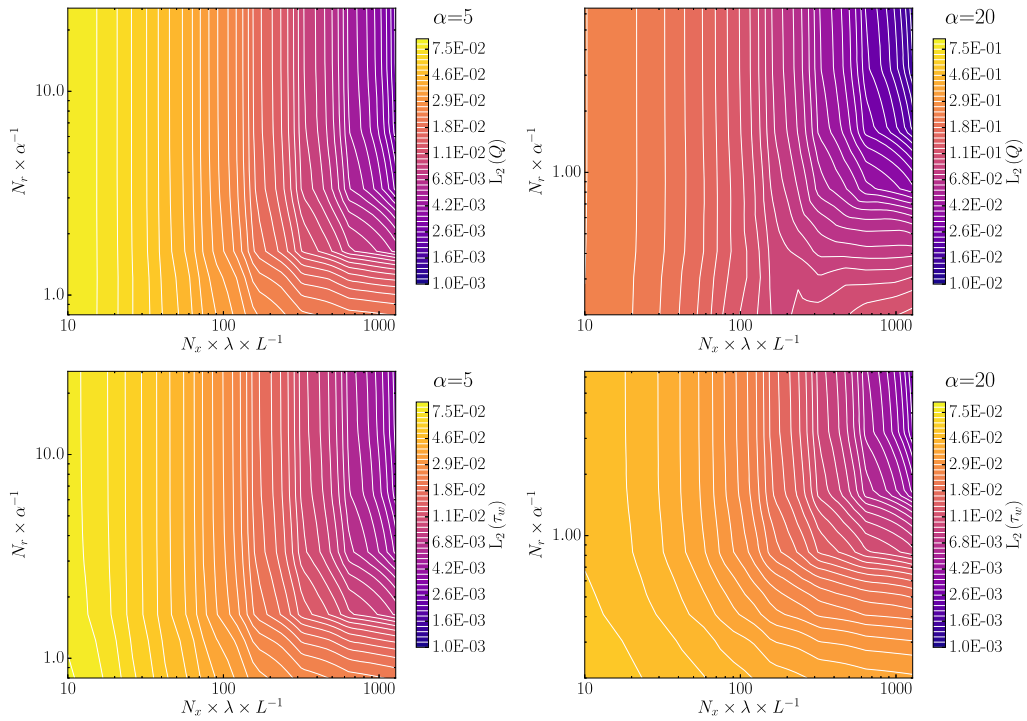\end{cases}
\tag{109}
$$

Fig. 4. Elastic Womersley example – Phase diagram of the evolution with $\bar{N}_x = \lambda N_x / L$ and with $\bar{N}_r = N_r / \alpha$ of the L_2 spatial error between the analytic Womersley and the multiring numerical solutions for the flow rate Q (top) and the WSS τ_w (bottom) for $\alpha = 5$ (left) and $\alpha = 20$ (right) at time $t = 0.3T_c + 11T_c$. At low values of $\bar{N}_x$, increasing $\bar{N}_r$ does not significantly decrease the L_2 error, whereas increasing $\bar{N}_x$ does. On the contrary, at high values of $\bar{N}_x$, increasing $\bar{N}_r$ significantly decreases the L_2 error, whereas increasing $\bar{N}_x$ does not. (For interpretation of the colors in this figure, the reader is referred to the web version of this article.)
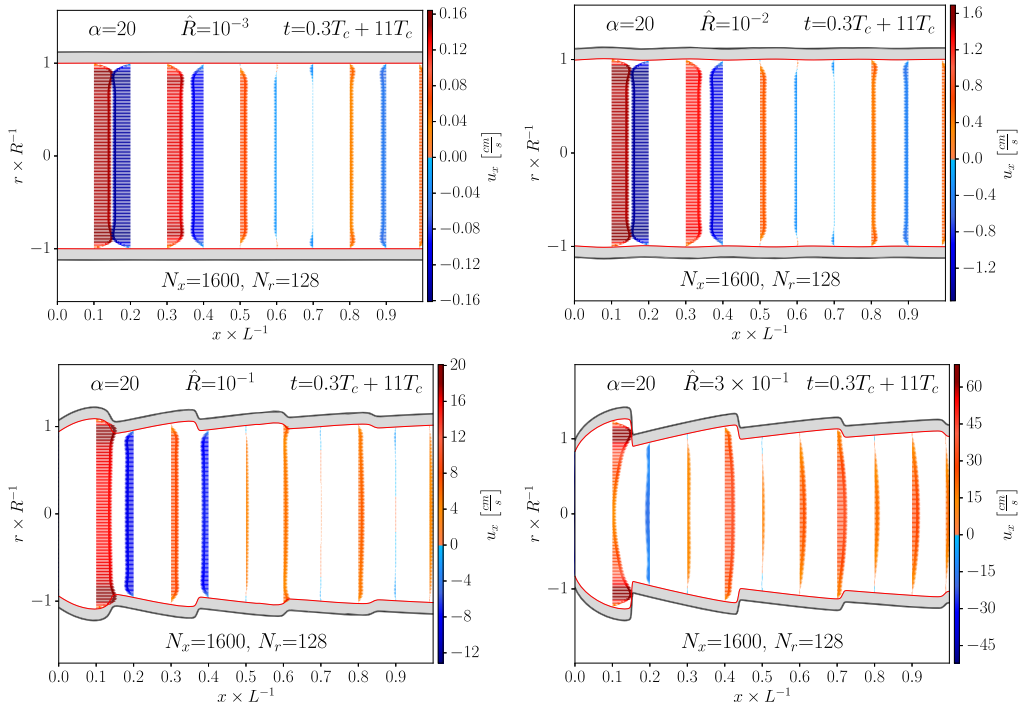
Fig. 5. Elastic Womersley example – Snapshots of the spatial evolution of the axial velocity u_x computed with the multiring model at $t = 0.3T_c + 11T_c$ using $N_x = 1600$ cells and $N_r = 128$ rings for $\alpha = 20$ and $\hat{R} \in \{10^{-3}, 10^{-2}, 10^{-1}, 3 \times 10^{-1}\}$. We observe that the multiring model is able to compute nonlinear flow behaviors with small and large wall deformations. (For interpretation of the colors in this figure, the reader is referred to the web version of this article.)

Table 2
Elastic Poiseuille example – Geometrical and mechanical parameters describing the artery and the inlet and outlet boundary conditions, given in the "cgs" unit system.

L	R_0	K	ρ	μ	$\hat{R}$	t_f
10	1	$\frac{10^2}{\sqrt{\pi}}$	1	1	10^{-1}	20
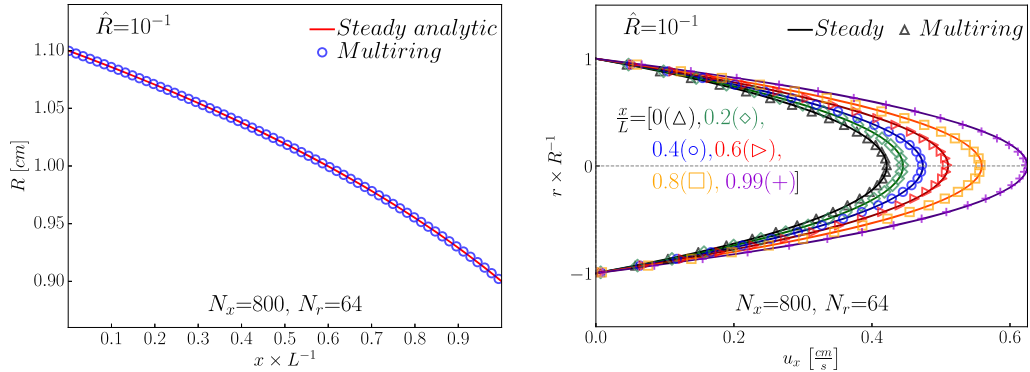
Fig. 6. Elastic Poiseuille example – Spatial evolution of the steady radius R (left) and the steady axial velocity profiles u_x (right) computed with the analytic Poiseuille solution (——) and the multiring model (marks) in $x \in \{0\,(\triangle),\, 0.2\,(\diamond),\, 0.4\,(\circ),\, 0.6\,(\triangleright),\, 0.8\,(\square),\, 0.99\,(+)\}L$ using $N_x = 800$ cells and $N_r = 64$ rings. We observe a good agreement between the Poiseuille and the multiring numerical solutions.

Table 3
Elastic Poiseuille example – Convergence of the L_1, L_2 and L_∞ spatial errors between the steady analytic Poiseuille solution and the steady multiring numerical solution for the radius R. We observe that the numerical solution converges at order 1, which is the expected order of convergence.

N_x	N_r	$L_1(R)$	Order	$L_2(R)$	Order	$L_\infty(R)$	Order
100	8	1.29×10^{-3}	–	7.35×10^{-4}	–	5.36×10^{-4}	–
200	16	5.93×10^{-4}	−0.56	3.37×10^{-4}	−0.56	2.46×10^{-4}	−0.56
400	32	2.25×10^{-4}	−0.70	1.27×10^{-4}	−0.70	9.33×10^{-5}	−0.70
800	64	4.54×10^{-5}	−1.15	2.49×10^{-5}	−1.18	2.05×10^{-5}	−1.09

In [37,59], the authors used this solution to validate their numerical code solving the axisymmetric RNS-P equations (1). We reproduce here this solution using the multiring model (23).

We consider a straight artery initially at rest (eq. (107)). We impose the pressure gradient by setting at the inlet and outlet constant pressures consistent with the analytic solution (109):

$$\begin{cases} p\,(x=0) = p_0 + \sqrt{\pi}\,K R_0 \hat{R} \\ p\,(x=L) = p_0 - \sqrt{\pi}\,K R_0 \hat{R}. \end{cases} \tag{110}$$

For simplicity we set $p_0 = 0$. The values of the geometrical and mechanical parameters describing the artery as well as those describing the inlet and outlet boundary conditions are presented in Table 2 and are given in the "cgs" unit system. The final simulation time t_f is chosen large enough to reach a steady flow regime and the value of $\hat{R}$ is chosen small enough such that the linear approximation required to obtain the elastic Poiseuille solution is valid.

In Fig. 6, we plot the spatial evolution of the steady radius R (Fig. 6 left) and the steady axial velocity profiles u_x (Fig. 6 right) computed with the analytic Poiseuille solution and the multiring model in $x \in \{0, 0.2, 0.4, 0.6, 0.8, 0.99\}L$. We use $N_x = 800$ cells and $N_r = 64$ rings. We observe that at each recorded position, the steady multiring numerical solution is in agreement with the steady analytic Poiseuille solution.

As the steady Poiseuille solution is smooth enough, we perform a convergence analysis to determine the order of accuracy of the multiring numerical scheme. We consider the following axial and radial mesh refinements $[N_x, N_r] \in \{[100, 8], [200, 16], [400, 32], [800, 64]\}$ and focus only on the numerical solution for the radius R for simplicity. In Table 3, we compute the L_1, L_2 and L_∞ spatial errors between the analytic Poiseuille solution and the steady multiring numerical solution for the radius R. We observe that the numerical solution converges at order 1, which is the expected order of convergence.

In the two previous examples, we have shown that the multiring model (23) is able to accurately capture steady and unsteady linear blood flow behaviors in a straight artery. We are therefore confident that the multiring model (23) can compute all relevant linear flow features encountered in large straight axisymmetric elastic arteries. However, the RNS-P system of equations (1) is a rich dynamical system that is not limited to describing linear harmonic and steady solutions in elastic arteries. In the following sections, we will continue to validate the multiring model, the numerical scheme and the boundary conditions using nonlinear steady examples in rigid arteries with varying geometrical and mechanical properties.

Table 4

Rigid Poiseuille example – Geometrical and mechanical parameters describing the artery and the inlet and outlet boundary conditions, given in the "cgs" unit system.

L	R_0	K	ρ	μ	U_{in}	R_t	t_f	$R_{e,R}$
$0.25 \, R_{e,R} R\|_{x=0}$	1	10^7	1	$\rho \frac{U_{in} R\|_{x=0}}{R_{e,R}}$	100	0	$0.5 \frac{R_{e,R} R\|_{x=0}}{U_{in}}$	100

7. Nonlinear examples in a rigid artery

7.1. Nonlinear transition from a flat to a Poiseuille velocity profile

In [21], the authors studied the behavior of the RNS-P equations (1) when computing steady flows in a rigid axisymmetric cylinder. They showed that RNS-P equations are able to describe the steady spatial transition from the Blasius [61] to the Poiseuille flow regime, starting from a flat velocity profile at the inlet and evolving towards a fully developed Poiseuille velocity profile at the outlet. We reproduce here this phenomenon using the multiring model (23). The relevant dimensionless number in this example is the Reynolds number $R_{e,R}$, defined as:

$$R_{e,R} = \frac{u_x R}{\nu}\bigg|_{x=0}, \tag{111}$$

and used to determine the relevant length and time scales in order to observe the steady spatial transition from the Blasius to the Poiseuille flow regime. Details on the determination of theses scales can be found in [21].

We consider a straight artery initially at rest (eq. (107)). We impose at the inlet a steady velocity profile. As we can not impose a flat velocity profile since it is not compatible with the no-slip boundary condition at the wall (21), we impose at the inlet a Von Kármán–Pohlhausen velocity profile [62], describing a fourth-order approximation of the axial velocity profile in the viscous boundary layer:

$$u_x (x=0, r, t) = U_{in} \, \phi_{Pohlhausen} (r), \tag{112}$$

where:

$$\phi_{Pohlhausen} (r) = \begin{cases} \dfrac{1 - [1-\eta]^3 \left[1 + \left[1 + \frac{\Delta}{6}\right]\eta\right]}{\frac{1}{30}\left[30 - 3\left[6 + \frac{\Delta}{6}\right]\delta_{BL} + \left[4 + \frac{\Delta}{6}\right]\delta_{BL}^2\right]} & \text{if } \eta < 1 \\[4mm] \dfrac{1}{\frac{1}{30}\left[30 - 3\left[6 + \frac{\Delta}{6}\right]\delta_{BL} + \left[4 + \frac{\Delta}{6}\right]\delta_{BL}^2\right]} & \text{if } \eta \geq 1, \end{cases} \tag{113}$$

with $\Delta = 12$ and $\eta = [1 - r/R]/\delta_{BL}$. The parameter δ_{BL} is the estimated width of the boundary layer, that we choose here equal to $\delta_{BL} = l_{r,N_r} + l_{r,N_r-1}$. We impose at the outlet a zero reflection coefficient R_t to remove any backward traveling waves. The values of the geometrical and mechanical parameters describing the artery as well as those describing the inlet and outlet boundary conditions are presented in Table 4 and are given in the "cgs" unit system. They mimic physiological conditions at the root of the aorta, where $R_{e,R} \approx 100$. The final simulation time t_f is chosen large enough to reach a steady flow regime. As the multiring model (23) is intrinsically elastic, it is not possible to exactly simulate the flow of blood in a rigid cylinder. Nevertheless, by artificially increasing the arterial wall rigidity K (here $K = 10^7$), we penalize the wall's displacement and place ourselves in a quasi-rigid wall configuration.

To assess the quality of the multiring numerical results, we compare them to those of the steady numerical code presented in [21]. This steady code was used to solve the steady RNS-P equations (1) in a rigid tube and compared well with the results of an integral interactive boundary layer (IBL) code. In the following examples, all results of the steady code used as reference solutions are obtained using $N_x = 50000$ cells in the axial direction and $N_r = 1000$ cells in the radial direction, which corresponds to a very fine mesh in both directions.

In Fig. 7, we plot the steady spatial evolution of the centerline velocity $u_x|_{r=0}$ (Fig. 7 left) and the pressure p (Fig. 7 right) computed with the reference solution and the multiring model. We use $N_x \in \{800, 1600, 3200\}$ cells and $N_r = 32$ rings. We observe that as we increase the number of cells N_x, the steady multiring numerical solution converges towards the steady reference solution and is able to describe the spatial transition from a flat velocity profile at the inlet to a Poiseuille velocity profile at the outlet. The number of cells N_x required to match the steady solution is relatively high since the transition from of flat to a Poiseuille velocity profile is a nonlinear phenomenon occurring on a short length scale (between $x = 0$ and $x = 0.15R_{e,R} R|_{x=0}$).

In Fig. 8, we represent the steady velocity profiles computed with the steady reference solution and the multiring model in $x \in \{0.005, 0.01, 0.025, 0.05, 0.1, 0.2\}R_{e,R} R|_{x=0}$. We use $N_x \in \{800, 3200\}$ cells and $N_r = 32$ rings. For each recorded position, the steady multiring numerical velocity profiles converge towards the steady reference velocity profiles as we increase the number of cells N_x. These results are coherent with the results presented in Fig. 7.
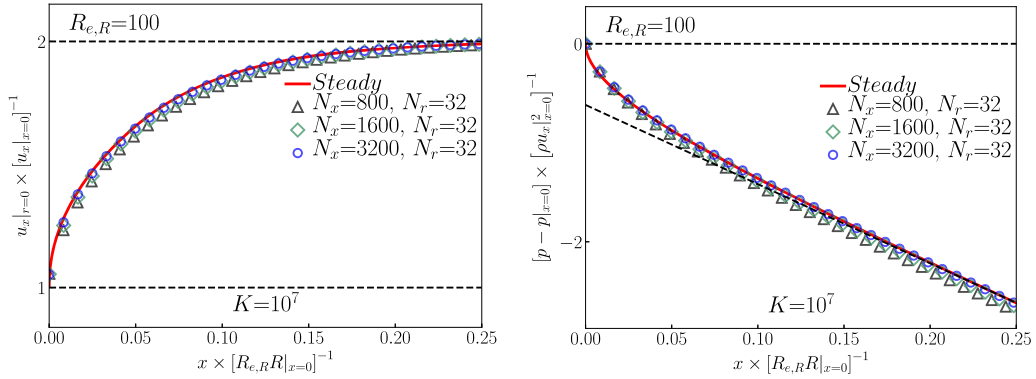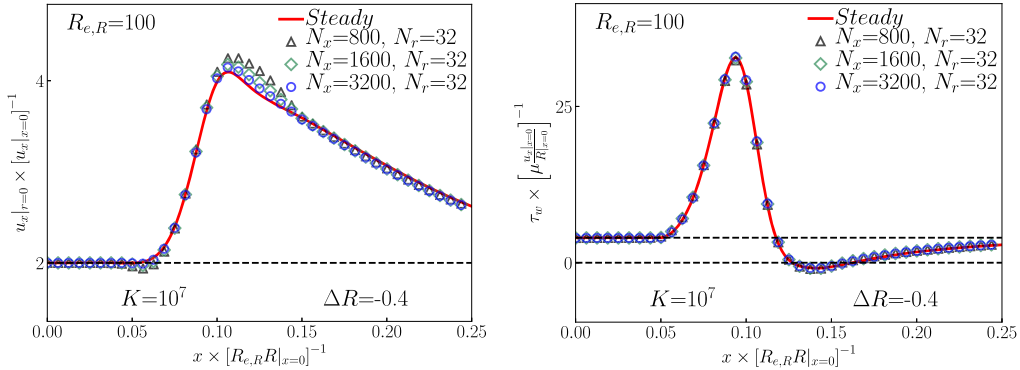
Fig. 7. Rigid Poiseuille example – Spatial evolution of the steady centerline velocity $u_x|_{r=0}$ (left) and the steady pressure p (right) computed with the steady reference solution [21] (———) and the multiring model (marks) using $N_x \in \{800 \, (\triangle), 1600 \, (\diamond), 3200 \, (\circ)\}$ cells and $N_r = 32$ rings. On the left plot, the dashed lines (— —) represent the values of the flat centerline velocity ($u_x|_{r=0} = u_x|_{x=0}$) and the Poiseuille centerline velocity ($u_x|_{r=0} = 2u_x|_{x=0}$). On the right plot, the dashed line (— —) represents the pressure drop $-8x/\left[R_{e,R}R|_{x=0}\right]$ of a Poiseuille flow. For each quantity, the steady multiring numerical solution converges towards the steady reference solution and we observe the transition from a flat to a Poiseuille velocity profile.
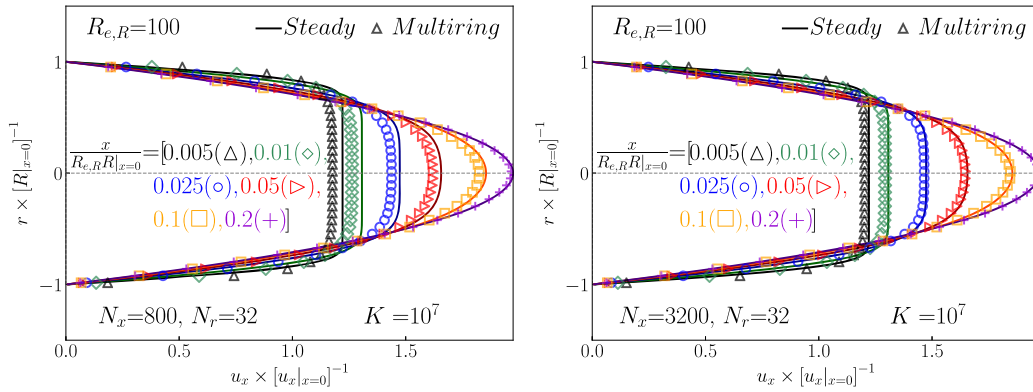
Fig. 8. Rigid Poiseuille example – Spatial evolution of the steady velocity profiles u_x computed with the steady reference solution [21] (———) and with the multiring model (marks) in $x \in \{0.005 \, (\triangle), 0.01 \, (\diamond), 0.025 \, (\circ), 0.05 \, (\triangleright), 0.1 \, (\square), 0.2 \, (+)\}R_{e,R}R|_{x=0}$ using $N_x \in \{800 \, (\text{left}), 3200 \, (\text{right})\}$ cells and $N_r = 32$ rings. We observe that the steady multiring velocity profiles converge towards the steady reference velocity profiles and accurately reproduce the transition from the Blasius to the Poiseuille flow regime.

7.2. Rigid wall stenosis and aneurysm

Stenoses and aneurysms are commonly encountered pathologies and correspond respectively to local constrictions and expansions of the neutral radius R_0 of the artery. The flow patterns in rigid stenoses and aneurysms have been studied by many authors [63–68]. In [21], the authors computed the numerical solution of the steady RNS-P equations (1) in an axisymmetric rigid artery presenting a stenosis. They used the steady code presented in the previous section and were able to compute flow recirculations in case of severe stenoses. We use here the multiring model (23) to compute the steady flow in a rigid stenosis and in a rigid aneurysm. As in the previous section, the relevant dimensionless number is the Reynolds number $R_{e,R}$ (111).

We consider an artery initially at rest (eq. (107)). We impose at the inlet a steady Poiseuille velocity profile:

$$u_x(x=0, r, t) = 2U_{in}\left[1 - \frac{r^2}{R^2}\right],\tag{114}$$

and at the outlet a zero reflection coefficient R_t to remove any backward traveling waves. The values of the geometrical and mechanical parameters describing the artery as well as those describing the inlet and outlet boundary conditions are presented in Table 5 and are given in the "cgs" unit system. They mimic physiological conditions at the root of the aorta, where $R_{e,R} \approx 100$. The final simulation time t_f is chosen large enough to reach a steady flow regime. The stenosis and aneurysm considered here are described by the following variation of the neutral radius R_0:

$$R_0 = \begin{cases} R_0 & \text{if } x < x_s \text{ or } x > x_f \\ R_0\left[1 + \frac{\Delta R}{2}\left[1 + \cos\left(\pi + 2\pi \frac{x - x_s}{x_f - x_s}\right)\right]\right] & \text{if } x_s \leq x \geq x_f. \end{cases}\tag{115}$$

Table 5
Rigid stenosis and aneurysm examples – Geometrical and mechanical parameters describing the artery and the inlet and outlet boundary conditions, given in the "cgs" unit system.

L	R_0	ΔR	K	ρ	μ	U_{in}	R_t	t_f	$R_{e,R}$
$0.25\ R_{e,R}R\vert_{x=0}$	1	± 0.4	10^7	1	$\rho\frac{U_{in}R\vert_{x=0}}{R_{e,R}}$	100	0	$0.5\frac{R_{e,R}R\vert_{x=0}}{U_{in}}$	100

Fig. 9. Rigid stenosis example – Spatial evolution of the steady centerline velocity $u_x\vert_{r=0}$ (left) and the steady WSS τ_w (right) computed with the steady reference solution [21] (—) and the multiring model (marks) using $N_x \in \{800\,(\triangle),\ 1600\,(\diamond),\ 3200\,(\circ)\}$ cells and $N_r = 32$ rings. On the left plot, the dashed line (– –) represents the value of the Poiseuille centerline velocity ($u_x\vert_{r=0} = 2u_x\vert_{x=0}$). On the right plot, the dashed line (– –) represents the value of the Poiseuille WSS ($\tau_w = 4\mu u_x\vert_{x=0}/R\vert_{x=0}$). For each quantity, the steady multiring numerical solution converges towards the steady reference solution.

We choose $x_s = \frac{L}{5}$ and $x_f = \frac{3L}{5}$ to satisfy the long-wave hypothesis. We set $\Delta R = -0.4$ to define the stenosis and $\Delta R = +0.4$ to define the aneurysm. As in the previous section, we artificially increase the arterial wall rigidity K (here $K = 10^7$) to penalize the wall's displacement and place ourselves in a quasi-rigid wall configuration.

As in the previous section, we compare the results of the multiring model (23) to those of the steady numerical code presented in [21]. In [25], this steady code was used to solve the steady RNS-P equations (1) in a rigid stenosis and compared well to the results of a *finite element* code for the incompressible Navier–Stokes equations. In the following examples, all results of the steady code used as reference solutions are obtained using $N_x = 50000$ cells in the axial direction and $N_r = 1000$ cells in the radial direction, which corresponds to a very fine mesh in both directions.

7.2.1. Flow in a stenosis

We first compute the steady flow in a rigid stenosis ($\Delta R = -0.4$). In Fig. 9, we plot the steady spatial evolution of the centerline velocity $u_x\vert_{r=0}$ (Fig. 9 left) and of the wall shear stress (WSS) τ_w (Fig. 9 right) computed with the steady reference solution and the multiring model. We use $N_x \in \{800, 1600, 3200\}$ cells and $N_r = 32$ rings. We observe that as we increase the number of cells N_x, the steady multiring numerical solution for the centerline velocity $u_x\vert_{r=0}$ converges towards the steady reference solution. On the contrary, the steady multiring numerical solution for the WSS τ_w is already converged for $N_x = 800$. Indeed, the number of rings N_r used is sufficient to obtain an accurate description of the shape of the velocity profile near the wall. We also note that the WSS τ_w becomes negative after the stenosis, indicating that the multiring model is able to capture flow recirculations. Finally, the steady WSS τ_w is similar to the one obtained in [69,23,70].

In Fig. 10, we represent the steady velocity profiles computed with the steady reference solution and the multiring model in $x \in \{0.05, 0.075, 0.1, 0.125, 0.15, 0.175\}R_{e,R}R\vert_{x=0}$. We use $N_x = 3200$ cells and $N_r = 32$ rings. For each recorded position, the steady multiring numerical velocity profiles agree well with t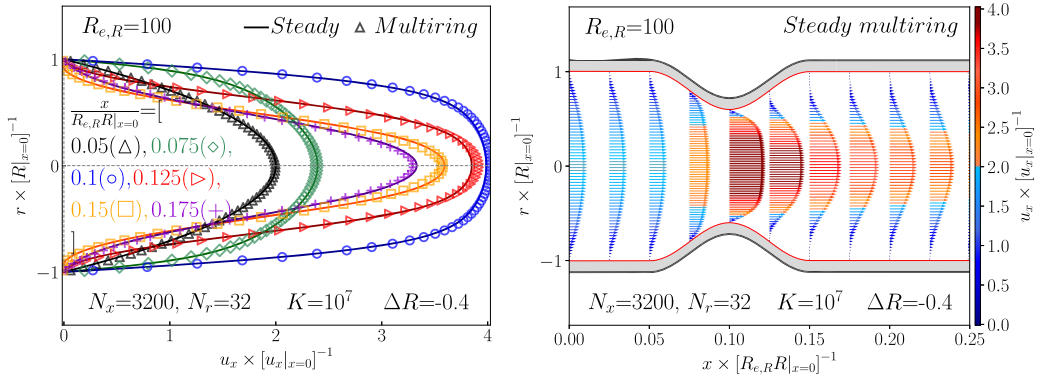he steady reference velocity profiles. We observe that after the stenosis, a small jet-like region of high velocities forms in the center of the artery and a region of low and negative velocities appears near the wall. These results are coherent with those presented in Fig. 9 and with the velocities profiles obtained in [69].

7.2.2. Flow in an aneurysm

We compute here the steady flow in a rigid aneurysm ($\Delta R = +0.4$). In Fig. 11, we plot the steady spatial evolution of the centerline velocity $u_x\vert_{r=0}$ (Fig. 11 left) and of the wall shear stress (WSS) τ_w (Fig. 11 right) computed with the steady reference solution and the multiring model. We use $N_x \in \{800, 1600, 3200\}$ cells and $N_r = 32$ rings. For each quantity, the steady multiring numerical solution converges towards the steady reference solution. We also note that even though the aneurysm is not large enough to create a flow recirculation, the WSS τ_w is almost negative in the center of the aneurysm. Finally, the steady WSS τ_w is similar to the one obtained in [71,72].

In Fig. 12, we represent the steady velocity profiles computed with the steady reference solution and the multiring model in $x \in \{0.05, 0.075, 0.1, 0.125, 0.15, 0.175\}R_{e,R}R\vert_{x=0}$. We use $N_x = 3200$ cells and $N_r = 32$ rings. For each recorded position, the steady multiring numerical velocity profiles agree well with the steady reference velocity profiles.

Fig. 10. Rigid stenosis example – Spatial evolution of the steady velocity profiles computed with the steady reference solution [21] (——) and the multiring model (marks) in $x \in \{0.05\,(\triangle),\ 0.075\,(\diamond),\ 0.1\,(\circ),\ 0.125\,(\triangleright),\ 0.15\,(\square),\ 0.175\,(+)\}R_{e,R}R|_{x=0}$ using $N_x = 3200$ cells and $N_r = 32$ rings. We observe that the multiring velocity profiles are in good accord with the steady reference velocity profiles.
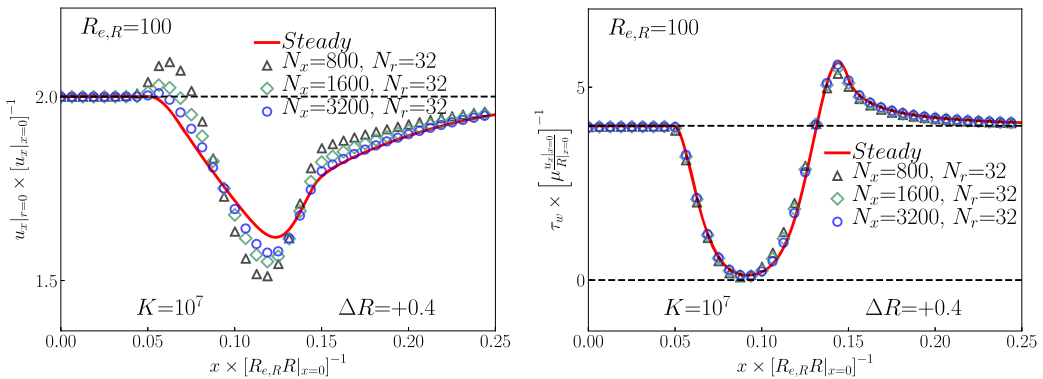

Fig. 11. Rigid aneurysm example – Spatial evolution of the steady centerline velocity $u_x|_{r=0}$ (left) and the steady WSS τ_w (right) computed with the reference solution [21] (——) and the multiring model (marks) using $N_x \in \{800\,(\triangle),\ 1600\,(\diamond),\ 3200\,(\circ)\}$ cells and $N_r = 32$ rings. On the left plot, the dashed line (– –) represents the value of the Poiseuille centerline velocity ($u_x|_{r=0} = 2u_x|_{x=0}$). On the right plot, the dashed line (– –) represents the value of the Poiseuille WSS ($\tau_w = 4\mu u_x|_{x=0}/R|_{x=0}$). For each quantity, the steady multiring numerical solution converges towards the steady reference solution.
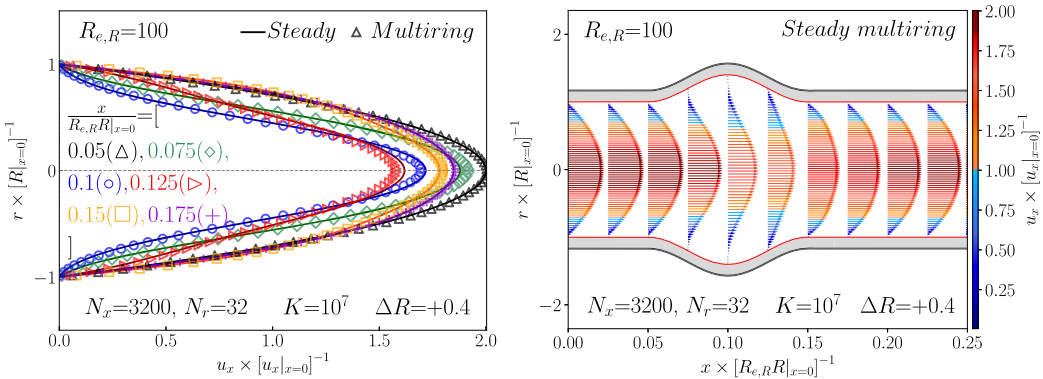

Fig. 12. Rigid aneurysm example – Spatial evolution of the steady velocity profiles computed with the reference solution [21] (——) and the multiring model (marks) in $x \in \{0.05\,(\triangle),\ 0.075\,(\diamond),\ 0.1\,(\circ),\ 0.125\,(\triangleright),\ 0.15\,(\square),\ 0.175\,(+)\}R_{e,R}R|_{x=0}$ using $N_x = 3200$ cells and $N_r = 32$ rings. We observe that the steady multiring velocity profiles are in good accord with the steady reference velocity profiles.

The results presented previously indicate that for a high arterial wall rigidity, the multiring model (23) is able to compute the characteristic steady nonlinear flow features in a rigid artery. Indeed, we have shown that it can describe the nonlinear steady transition from a flat to a Poiseuille velocity profile, the acceleration of the flow in a stenosis, the deceleration of the flow in a aneurysm as well as small flow recirculations after the stenosis. It can also correctly compute the variation of the WSS and the pressure. These results show that the multiring model (23) correctly describes all relevant steady and unsteady nonlinear blood flow features in quasi-rigid straight, constricted (stenosis) and expanded (aneurysm) arteries. Next, we use the multiring model to compute the unsteady blood flow in an elastic stenosis.

Table 6
Elastic artery example – Geometrical and mechanical parameters describing the artery and the inlet and outlet boundary conditions, given in the "cgs" unit system.

L	R_0	ΔR	K	ρ	μ	U_{in}	R_t	T_c	t_f	$R_{e,R}$	α	S_h
$0.25 \ R_{e,R}R\|_{x=0}$	1	$\{0, -0.4\}$	10^5	1	$\rho \frac{U_{in}R\|_{x=0}}{R_{e,R}}$	$S_h c$	0	$\frac{2\pi}{\nu}\frac{R_0^2}{\alpha^2}$	$5T_c$	100	15	10^{-2}

8. Unsteady flow in an elastic straight and stenosed artery

In physiological conditions, the arteries are elastic and the flow of blood is pulsatile. We propose here to compute with the multiring model (23) a periodic flow in straight and stenosed elastic arteries and to systematically compare the flow features computed in both configurations. The Womersley number α (100), the Reynolds number $R_{e,R}$ (111) and the Shapiro number S_h (38) are the relevant dimensionless numbers in this example. Here S_h is defined as:

$$S_h = \frac{U_{in}}{c} \quad \text{with} \quad c = \sqrt{\sqrt{\pi}\frac{K}{2\rho}R}. \tag{116}$$

We consider an artery initially at rest (eq. (107)). We impose at the inlet a periodic Pohlhausen velocity profile (113) mimicking the flow ejected by the heart in the aorta:

$$u_x(x=0, r, t) = U_{in}\, \phi_{Polhlausen}(r)\max\left(0, \sin\left(2\pi\frac{t}{T_c}\right)\right), \tag{117}$$

where T_c is the period of the flow. Note that blood is injected in the artery for only half a period, such that this test case is not strictly equivalent to the Womersley solution presented in the previous sections. At the outlet, we impose a zero reflection coefficient R_t to remove any backward traveling waves and highlight only the flow perturbations induced by the stenosis. The values of the geometrical and mechanical parameters describing the artery as well as those describing the inlet and outlet boundary conditions are presented in Table 6 and are given in the "cgs" unit system. They mimic physiological conditions at the root of the aorta, where $R_{e,R} \approx 100$, $\alpha \approx 15$ and $S_h \approx 10^{-2}$. The final simulation time t_f is chosen large enough to reach a periodic flow regime. As in the previous section, the stenosis is described by the neutral radius R_0 (115) with $x_s = \frac{L}{5}$, $x_f = \frac{3L}{5}$ and $\Delta R = -0.4$. The straight artery is obtained by choosing $\Delta R = 0$.

In Fig. 13, we plot the time variations for $4T_c \leq t \leq 5T_c$ of the pressure p (Fig. 13 top), the flow rate Q (Fig. 13 middle top), the pressure gradient $\nabla_x p$ (Fig. 13 middle bottom) and the WSS τ_w (Fig. 13 bottom) computed with the multiring model in the straight ($\Delta R = 0$) and stenosed ($\Delta R = -0.4$) arteries in $x \in \{0.025 \,(\text{left}), 0.1 \,(\text{center}), 0.225 \,(\text{right})\}R_{e,R}R\|_{x=0}$. We use $N_x = 3200$ cells and $N_r = 32$ rings. In the straight artery configuration ($\Delta R = 0$), we observe characteristic features of the unperturbed propagation of the elastic pulse wave from the inlet to the outlet. Indeed, the time variations of the different variables are identical at each recorded position but occur with an increasing delay as the wave moves away from the inlet at the finite wave speed c (37). In the stenosed artery configuration ($\Delta R = -0.4$), we observe similar wave propagation behaviors with added perturbations due to the presence of the stenosis. During systole ($4T_c \leq t \leq 4.5T_c$), the maximum amplitude of the pressure waveform is higher than in the straight configuration before the stenosis, in $x = 0.025R_{e,R}R\|_{x=0}$, whereas the maximum amplitude of the flow waveform is higher after the stenosis, in $x = 0.225R_{e,R}R\|_{x=0}$. At the begin of diastole ($4.5T_c \leq t \leq 4.7T_c$) at each recorded position in the stenosed artery configuration, the pressure becomes negative and the flow reverses whereas these quantities are zero in the straight artery configuration as the wave has already exited the artery. These behaviors during systole and diastole are evidence of wave reflection and transmission phenomena caused by the presence of the stenosis. Additionally, the stenosis induces a flow acceleration, which is highlighted by larger variations of the pressure gradient $\nabla_x p$ and the WSS τ_w than in the straight configuration in the middle of the stenosis, in $x = 0.1R_{e,R}R\|_{x=0}$. Finally, we note that in both the straight and stenosed arteries, the WSS τ_w becomes negative during diastole ($4.5T_c \leq t \leq 5T_c$), which is evidence of flow reversal and recirculation.

To better understand the flow perturbations induced by the stenosis, we decompose in Fig. 14 the flow motion over the fourth period ($4T_c \leq t \leq 5T_c$) and focus on three different instants of the cycle: the peak of systole at $t = 0.2T_c + 4T_c$, the end of systole (or the beginning of diastole) at $t = 0.6T_c + 4T_c$ and the end of diastole at $t = 0.9T_c + 4T_c$. For each instant, we plot the velocity profiles in the straight ($\Delta R = 0$, Fig. 14 top) and stenosed ($\Delta R = -0.4$, Fig. 14 middle) arteries and compare in these two configurations the velocity profiles in $x = \{0.025, 0.1, 0.225\}R_{e,R}R\|_{x=0}$ (Fig. 14 bottom). In Fig. 14 bottom, we observe that the velocity profiles taken in $x = \{0.025, 0.225\}R_{e,R}R\|_{x=0}$ are almost identical in the straight and stenosed arteries, indicating that the stenosis does not induce strong perturbations of the shape and amplitude of the velocity profiles at these positions. On the contrary, they differ in $x = 0.1R_{e,R}R\|_{x=0}$ as the constriction creates a flow acceleration which has already been observed in Fig. 13. Finally, at times $t = 0.6T_c + 4T_c$ and $t = 0.9T_c + 4T_c$, we observe that the pulse wave has left the artery and that the flow relaxes towards its equilibrium state. The velocity amplitude decreases as we reach the end of diastole, with positive velocities in the center of the artery, in $r = 0$, and negative velocities near the wall, highlighted by the negative WSS τ_w in Fig. 13. Indeed, in Fig. 13, we see that for $0.3T_c + 4T_c \leq t \leq 0.6T_c + 4T_c$, the pressure gradient is positive, which reverses the flow only near the wall as the flow inertia in the core of the artery is too strong.
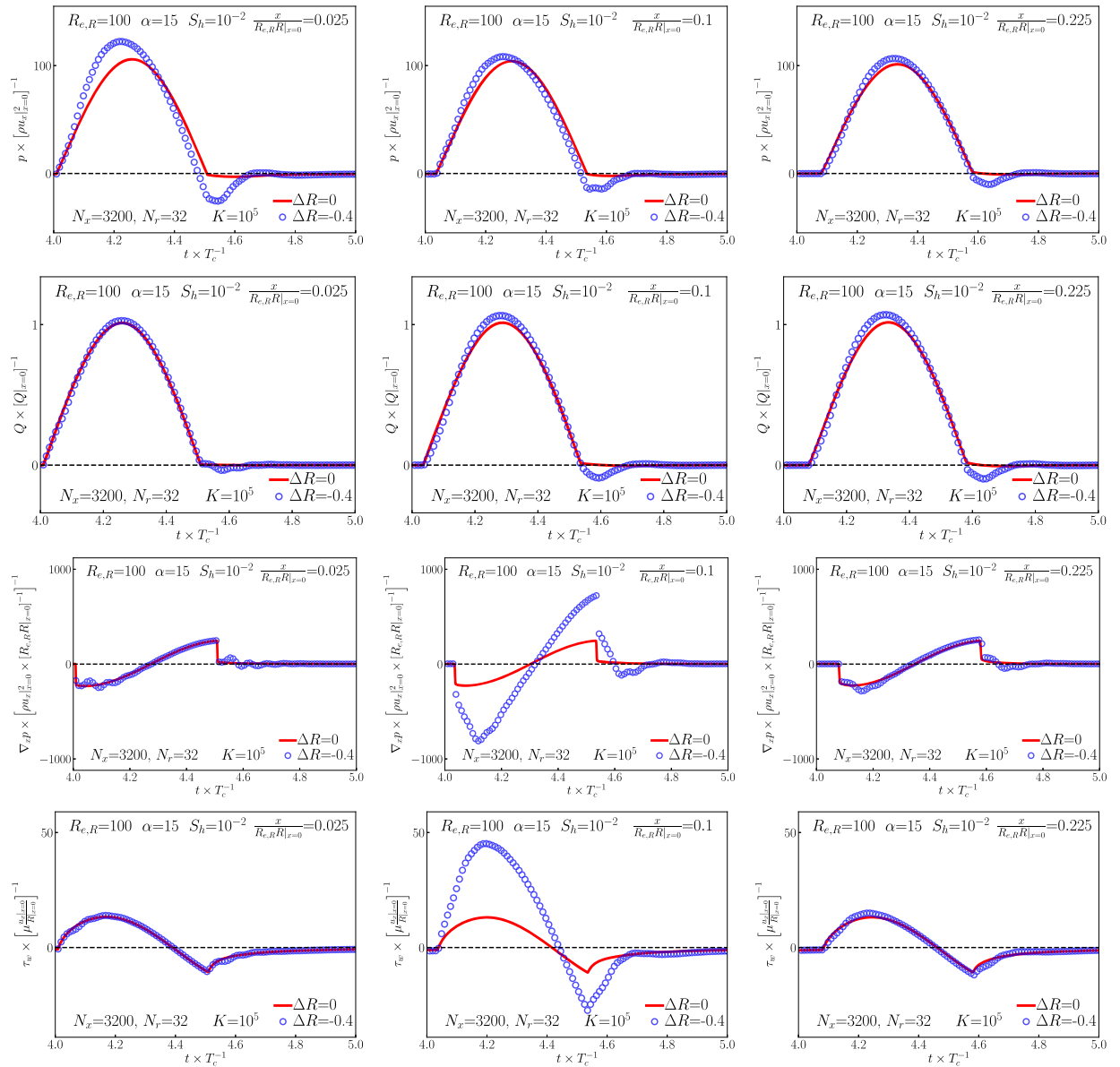
Fig. 13. Elastic artery example – Time variations for $4T_c \leq t \leq 5T_c$ of the pressure p (top), the flow rate Q (middle top), the pressure gradient $\nabla_x p$ (middle bottom) and the WSS τ_w (bottom) computed with the multiring model in the straight (——) and stenosed (○) arteries in $x \in \{0.025$ (left), 0.1 (center), 0.225 (right)$\}R_{e,R}R|_{x=0}$ using $N_x = 3200$ cells and $N_r = 32$ rings. We observe evidence of wave propagation and reflection as well as flow reversal and recirculation.

The results presented in Figs. 13 and 14 are similar to those obtained in [73]. They indicate that the multiring model (23) is capable of describing unsteady flows and wave propagation in a elastic stenosis and that this model can compute the expected unsteady flow behaviors such as wave reflections and flow recirculations.

9. Conclusion

We have presented a two-dimensional (2D) nonlinear axisymmetric multiring model to compute blood flow in elastic arteries. This model results from the integration of the RNS-P equations (1) over concentric rings of fluid in an elastic artery, providing a unified framework where both the motion of the fluid and the displacement of the arterial wall are dealt with simultaneously. Its mathematical structure as a system of balance laws has allowed us to use a robust, conservative and positive *finite volume* numerical method to compute steady and unsteady linear and nonlinear flows in quasi-rigid and elastic arteries. The multiring model and the numerical method were validated on multiple physiological blood flow examples. For each of the considered test cases, the multiring solution agreed very well with the reference solution for
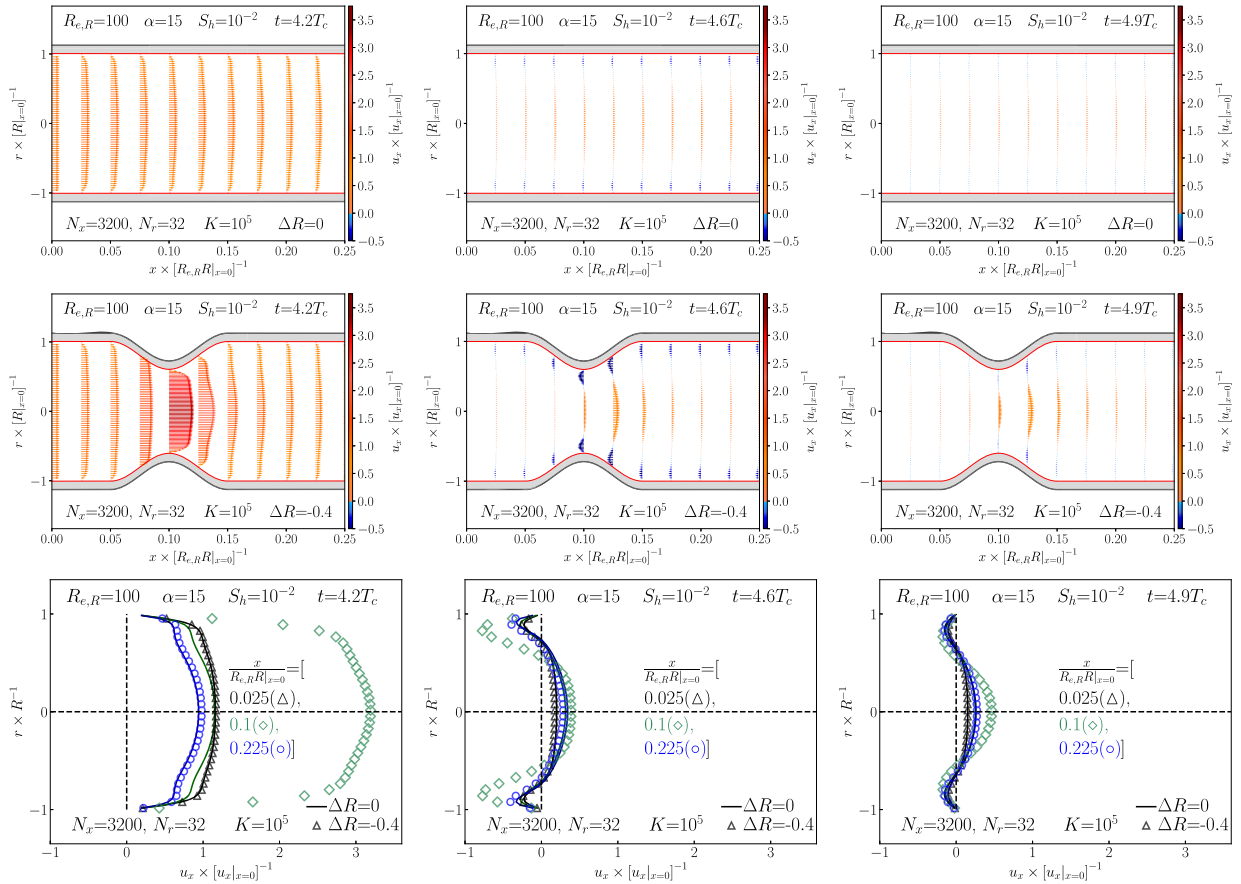
Fig. 14. Elastic artery example – Snapshots at times $t \in \{0.2, 0.6, 0.9\}T_c + 4T_c$ of the spatial evolution of the axial velocity u_x in the straight (top) and stenosed (middle) arteries and comparison of the axial velocity profiles u_x in the straight (——) and stenosed (marks) arteries in $x = \{0.025 (\triangle), 0.1 (\diamond), 0.225 (\circ)\}R_{e,R}R|_{x=0}$ (bottom), computed with the multiring model using $N_x = 3200$ cells and $N_r = 32$ rings. In $x = \{0.025, 0.225\}R_{e,R}R|_{x=0}$, we observe almost no difference between the straight and stenosed velocity profiles. On the contrary, in $x = 0.1R_{e,R}R|_{x=0}$, we see a flow acceleration due to the constriction. At times $t \in \{0.6, 0.9\}T_c + 4T_c$, backflow is created near the wall in the straight and stenosed arteries due to the positive pressure gradient occurring at $0.3T_c + 4T_c \le t \le 0.6T_c + 4T_c$. However, the inertia in the core of the artery is too strong to observe a complete flow reversal in one period.

the velocity profiles, the wall shear stress (WSS) and other averaged quantities such as the flow rate or the pressure, even when large arterial wall deformations were considered. In the presence of pathologies such as stenoses or aneurysms, the multiring model captured the expected flow behaviors, and in particular flow recirculation, downstream of the stenosis and in the aneurysm. In comparison, classical one-dimensional (1D) models can only compute average quantities such as the flow rate or the pressure and can not describe flow recirculations. This study shows that the multiring model can serve as a superior alternative to 1D models to accurately compute blood flow in large elastic arteries at a reduced computational cost and could also prove to be a reliable substitute to three-dimensional (3D) models when simple arterial configurations are considered. This method can be extended to other pressure laws to describe the flow in veins and viscoelastic tubes or the propagation of a water hammer wave (Allevi's equation). In future works, we plan to couple the 2D multiring model with a 1D model and to propose a non-Newtonian 2D multiring model to take into account the effect of aggregation of red blood cells in regions of low shear rate.

Acknowledgements

References

[1] A. Quarteroni, A. Veneziani, C. Vergara, Geometric multiscale modeling of the cardiovascular system, between theory and practice, Comput. Methods Appl. Mech. Eng. 302 (2016) 193–252.
[2] G. Holzapfel, T. Gasser, R. Ogden, A new constitutive framework for arterial wall mechanics and a comparative study of material models, J. Elast. Phys. Sci. Solids 61 (1–3) (2000) 1–48.
[3] T. Hughes, W. Liu, T. Zimmermann, Lagrangian–Eulerian finite element formulation for incompressible viscous flows, Comput. Methods Appl. Mech. Eng. 29 (3) (1981) 329–349.

[4] C. Farhat, P. Geuzaine, C. Grandmont, The discrete geometric conservation law and the nonlinear stability of ALE schemes for the solution of flow problems on moving grids, J. Comput. Phys. 174 (2) (2001) 669–694.

[5] T. Tezduyar, Computation of moving boundaries and interfaces and stabilization parameters, Int. J. Numer. Methods Fluids 43 (5) (2003) 555–575.

[6] C. Figueroa, I. Vignon-Clementel, K. Jansen, T. Hughes, C. Taylor, A coupled momentum method for modeling blood flow in three-dimensional deformable arteries, Comput. Methods Appl. Mech. Eng. 195 (41) (2006) 5685–5706.

[7] T. Tezduyar, S. Sathe, T. Cragin, B. Nanna, B. Conklin, J. Pausewang, M. Schwaab, Modelling of fluid–structure interactions with the space–time finite elements: arterial fluid mechanics, Int. J. Numer. Methods Fluids 54 (6–8) (2007) 901–922.

[8] M. Mayr, T. Klöppel, W. Wall, M. Gee, A temporal consistent monolithic approach to fluid–structure interaction enabling single field predictors, SIAM J. Sci. Comput. 37 (1) (2015) B30–B59.

[9] C. Taylor, T. Hughes, C. Zarins, Finite element modeling of blood flow in arteries, Comput. Methods Appl. Mech. Eng. 158 (1) (1998) 155–196.

[10] I. Vignon-Clementel, A. Marsden, J. Feinstein, A primer on computational simulation in congenital heart disease for the clinician, Prog. Pediatr. Cardiol. 30 (1) (2010) 3–13.

[11] S. Sankaran, M. Moghadam, A. Kahn, E. Tseng, J. Guccione, A. Marsden, Patient-specific multiscale modeling of blood flow for coronary artery bypass graft surgery, Ann. Biomed. Eng. 40 (10) (2012) 2228–2242.

[12] J. Alastruey, K. Parker, J. Peiró, S. Sherwin, Analysing the pattern of pulse waves in arterial networks: a time-domain study, J. Eng. Math. 64 (4) (2009) 331–351.

[13] M. Politi, A. Ghigo, J. Fernández, I. Khelifa, J. Gaudric, J.-M. Fullana, P.-Y. Lagrée, The dicrotic notch analyzed by a numerical model, Comput. Biol. Med. 72 (2016) 54–64.

[14] N. Xiao, J. Humphrey, C. Figueroa, Multi-scale computational model of three-dimensional hemodynamics within a deformable full-body arterial network, J. Comput. Phys. 244 (2013) 22–40.

[15] H. Kim, I. Vignon-Clementel, J. Coogan, C. Figueroa, K. Jansen, C. Taylor, Patient-specific modeling of blood flow and pressure in human coronary arteries, Ann. Biomed. Eng. 38 (10) (2010) 3195–3209.

[16] L. Müller, E. Toro, A global multiscale mathematical model for the human circulation with emphasis on the venous system, Int. J. Numer. Methods Biomed. Eng. 30 (7) (2014) 681–725.

[17] A. Ramachandra, A. Kahn, A. Marsden, Patient-specific simulations reveal significant differences in mechanical stimuli in venous and arterial coronary grafts, J. Cardiovasc. Translat. Res. 9 (4) (2016) 279–290.

[18] C. Arthurs, K. Lau, K. Asrress, S. Redwood, C. Figueroa, A mathematical model of coronary blood flow control: simulation of patient-specific three-dimensional hemodynamics during exercise, Am. J. Physiol., Heart Circ. Physiol. 310 (9) (2016) H1242–H1258.

[19] C. Audebert, P. Bucur, M. Bekheit, E. Vibert, I. Vignon-Clementel, J.-F. Gerbeau, Kinetic scheme for arterial and venous blood flow, and application to partial hepatectomy modeling, Comput. Methods Appl. Mech. Eng. 314 (2017) 102–125.

[20] L. Prandtl, Motion of Fluids with Very Little Viscosity, Technical Memorandum 452, 1928.

[21] P.-Y. Lagrée, S. Lorthois, The RNS/Prandtl equations and their link with other asymptotic descriptions: application to the wall shear stress scaling in a constricted pipe, Int. J. Eng. Sci. 43 (3) (2005) 352–378.

[22] J. Womersley, XXIV. Oscillatory motion of a viscous liquid in a thin-walled elastic tube, I: the linear approximation for long waves, Lond. Edinb. Dublin Philos. Mag. J. Sci. 46 (373) (1955) 199–221.

[23] F. Smith, Flow through constricted or dilated pipes and channels: part 2, Q. J. Mech. Appl. Math. 29 (3) (1976) 365–376.

[24] G. Barrenechea, F. Chouly, A finite element method for the resolution of the reduced Navier–Stokes/Prandtl equations, Z. Angew. Math. Mech. 89 (1) (2009) 54–68.

[25] F. Chouly, P.-Y. Lagrée, Comparison of computations of asymptotic flow models in a constricted channel, Appl. Math. Model. 36 (12) (2012) 6061–6071.

[26] L. Euler, Principia pro motu sanguinis per arterias determinando, Opera Posth. Math. Phys. Ann. (1844) 814–823.

[27] J. Lambert, On the nonlinearities of fluid flow in nonrigid tubes, J. Franklin Inst. 266 (2) (1958) 83–102.

[28] L. Formaggia, D. Lamponi, A. Quarteroni, One-dimensional models for blood flow in arteries, J. Eng. Math. 47 (3–4) (2003) 251–276.

[29] L. Müller, C. Parés, E. Toro, Well-balanced high-order numerical schemes for one-dimensional blood flow in vessels with varying mechanical properties, J. Comput. Phys. 242 (2013) 53–85.

[30] X.-F. Wang, J.-M. Fullana, P.-Y. Lagrée, Verification and comparison of four numerical schemes for a 1D viscoelastic blood flow model, Comput. Methods Biomech. Biomed. Eng. 18 (15) (2015) 1704–1725.

[31] S. Čanić, D. Lamponi, A. Mikelic, J. Tambača, Self-consistent effective equations modeling blood flow in medium-to-large compliant arteries, Multiscale Model. Simul. 3 (3) (2005) 559–596.

[32] S. Čanić, C. Hartley, D. Rosenstrauch, J. Tambača, G. Guidoboni, A. Mikelić, Blood flow in compliant arteries: an effective viscoelastic reduced model, numerics, and experimental validation, Ann. Biomed. Eng. 34 (4) (2006) 575–592.

[33] D. Bessems, M. Rutten, F. van De Vosse, A wave propagation model of blood flow in large vessels using an approximate velocity profile function, J. Fluid Mech. 580 (2007) 145–168.

[34] P.-Y. Lagrée, An inverse technique to deduce the elasticity of a large artery, Eur. Phys. J. Appl. Phys. 9 (02) (2000) 153–163.

[35] J. Flores, J. Alastruey, E. Poiré, A novel analytical approach to pulsatile blood flow in the arterial network, Ann. Biomed. Eng. (2016) 1–22.

[36] S. Ling, H. Atabek, A nonlinear analysis of pulsatile flow in arteries, J. Fluid Mech. 55 (03) (1972) 493–511.

[37] V. Casulli, M. Dumbser, E. Toro, Semi-implicit numerical modeling of axially symmetric flows in compliant arterial systems, Int. J. Numer. Methods Biomed. Eng. 28 (2) (2012) 257–272.

[38] E. Audusse, M.-O. Bristeau, B. Perthame, J. Sainte-Marie, A multilayer Saint-Venant system with mass exchanges for shallow water flows: derivation and numerical validation, Modél. Math. Anal. Numér. 45 (01) (2011) 169–200.

[39] S. Sherwin, L. Formaggia, J. Peiro, V. Franke, Computational modeling of 1D blood flow with variable mechanical properties and its application to the simulation of wave propagation in the human arterial system, Int. J. Numer. Methods Fluids 43 (6–7) (2003) 673–700.

[40] M. Saito, Y. Ikenaga, M. Matsukawa, Y. Watanabe, T. Asada, P.-Y. Lagrée, One-dimensional model for propagation of a pressure wave in a model of the human arterial network: comparison of theoretical and experimental results, J. Biomech. Eng. 133 (12) (2011) 121005.

[41] A. Ghigo, O. Delestre, J.-M. Fullana, P.-Y. Lagrée, Low-Shapiro hydrostatic reconstruction technique for blood flow simulation in large arteries with varying geometrical and mechanical properties, J. Comput. Phys. 331 (2017) 108–136.

[42] A. Moens, Die Pulskurve, E.J. Brill, 1878.

[43] D. Korteweg, Über die Fortpflanzungsgeschwindigkeit des Schalles in elastischen Röhren, Ann. Phys. 241 (12) (1878) 525–542.

[44] A. Shapiro, Steady flow in collapsible tubes, J. Biomech. Eng. 99 (3) (1977) 126–147.

[45] A. Siviglia, M. Toffolon, Steady analysis of transcritical flows in collapsible tubes with discontinuous mechanical properties: implications for arteries and veins, J. Fluid Mech. 736 (2013) 195–215.

[46] E. Audusse, F. Benkhaldoun, S. Sari, M. Seaid, P. Tassi, A fast finite volume solver for multi-layered shallow water flows with mass exchange, J. Comput. Phys. 272 (2014) 23–45.

[47] E. Fernández-Nieto, E. Koné, T. De Luna, R. Bürger, A multilayer shallow water system for polydisperse sedimentation, J. Comput. Phys. 238 (2013) 281–314.

[48] F. Bouchut, Construction of BGK models with a family of kinetic entropies for a given system of conservation laws, J. Stat. Phys. 95 (1–2) (1999) 113–170.
[49] P. Roe, Upwind differencing schemes for hyperbolic conservation laws with source terms, in: Nonlinear hyperbolic problems, Springer, 1987, pp. 41–51.
[50] A. Bermúdez, M. Vázquez, Upwind methods for hyperbolic conservation laws with source terms, Comput. Fluids 23 (8) (1994) 1049–1071.
[51] L. Gosse, A.-Y. LeRoux, Un schéma-équilibre adapté aux lois de conservation scalaires non-homogènes, C. R. Math. Acad. Sci. 323 (5) (1996) 543–546.
[52] J. Greenberg, A.-Y. LeRoux, A well-balanced scheme for the numerical processing of source terms in hyperbolic equations, SIAM J. Numer. Anal. 33 (1) (1996) 1–16.
[53] E. Audusse, M.-O. Bristeau, A well-balanced positivity preserving second-order scheme for shallow water flows on unstructured meshes, J. Comput. Phys. 206 (1) (2005) 311–333.
[54] Delestre, P.-Y. Lagrée, A "well-balanced" finite volume scheme for blood flow simulation, Int. J. Numer. Methods Fluids 72 (2) (2013) 177–205.
[55] Delestre, A. Ghigo, J.-M. Fullana, P.-Y. Lagrée, A shallow water with variable pressure model for blood flow simulation, Netw. Heterog. Media 11 (1) (2016) 69–87.
[56] R. Courant, K. Friedrichs, H. Lewy, On the partial difference equations of mathematical physics, IBM J. 11 (2) (1967) 215–234.
[57] L. Thomas, Elliptic Problems in Linear Difference Equations over a Network, Watson Sci. Comput. Lab. Rept, Columbia University, New York, 1949, p. 1.
[58] M.-O. Bristeau, B. Coussin, Boundary conditions for the shallow water equations solved by kinetic schemes, 2001.
[59] M. Dumbser, U. Iben, M. Ioriatti, An efficient semi-implicit finite volume method for axially symmetric compressible flows in compliant tubes, Appl. Numer. Math. 89 (2015) 24–44.
[60] Y. Fung, Biomechanics: Circulation, Springer Science & Business Media, 2013.
[61] H. Schlichting, Boundary-Layer Theory, McGraw–Hill, 1968.
[62] K. Pohlhausen, Zur näherungsweisen Integration der Differentialgleichung der laminaren Grenzschicht, Z. Angew. Math. Mech. 1 (4) (1921) 252–290.
[63] S. Wille, Pulsatile pressure and flow in an arterial aneurysm simulated in a mathematical model, J. Biomed. Eng. 3 (2) (1981) 153–158.
[64] S. Wille, L. Walløe, Pulsatile pressure and flow in arterial stenoses simulated in a mathematical model, J. Biomed. Eng. 3 (1) (1981) 17–24.
[65] K. Perktold, On the paths of fluid particles in an axisymmetrical aneurysm, J. Biomech. 20 (3) (1987) 311–317.
[66] P. Di Achille, G. Tellides, C. Figueroa, J. Humphrey, A haemodynamic predictor of intraluminal thrombus formation in abdominal aortic aneurysms, Proc. R. Soc. A, vol. 470, The Royal Society, 2014, p. 20140163.
[67] A. Zaman, N. Ali, O. Bég, Numerical simulation of unsteady micropolar hemodynamics in a tapered catheterized artery with a combination of stenosis and aneurysm, Med. Biol. Eng. Comput. (2015) 1–14.
[68] L. Wang, B. Shi, Z. Chai, A lattice Boltzmann study of the asymmetry effect on the hemodynamics in stented fusiform aneurysms, Comput. Math. Appl. 71 (1) (2016) 328–348.
[69] B. Morgan, D. Young, An integral method for the analysis of flow in arterial stenoses, Bull. Math. Biol. 36 (1974) 39–53.
[70] J. Siegel, C. Markou, D. Ku, S. Hanson, A scaling law for wall shear rate through an arterial stenosis, J. Biomech. Eng. 116 (4) (1994) 446–451.
[71] R. Budwig, D. Elger, H. Hooper, J. Slippy, Steady flow in abdominal aortic aneurysm models, J. Biomech. Eng. 115 (4A) (1993) 418–423.
[72] E. Finol, C. Amon, Flow-induced wall shear stress in abdominal aortic aneurysms, part I: steady flow hemodynamics, Comput. Methods Biomech. Biomed. Eng. 5 (4) (2002) 309–318.
[73] D. Young, N. Cholvin, A. Roth, Pressure drop across artificially induced stenoses in the femoral arteries of dogs, Circ. Res. 36 (6) (1975) 735–743.